JGR Space Physics

RESEARCH ARTICLE
10.1029/2022JA030429

Key Points:

- Storm time medium-scale traveling ionospheric disturbances occur regularly near the base of storm-enhanced density in the continental US
- Disturbance wavefronts developed primarily during storm main phase at evening–midnight local times, elongated NW-SE, and traveled southwestward
- Disturbance onset coincided with intense electric fields and zonal propagation was synchronized with enhanced westward thermospheric winds

Supporting Information:

Supporting Information may be found in the online version of this article.

Correspondence to:

S.-R. Zhang,
shunrong@mit.edu

Citation:

Zhang, S.-R., Nishimura, Y., Erickson, P. J., Aa, E., Kil, H., Deng, Y., et al. (2022). Traveling ionospheric disturbances in the vicinity of storm-enhanced density at midlatitudes. *Journal of Geophysical Research: Space Physics*, *127*, e2022JA030429. https://doi.org/10.1029/2022JA030429

Received 2 MAR 2022
Accepted 27 JUL 2022

Traveling Ionospheric Disturbances in the Vicinity of Storm-Enhanced Density at Midlatitudes

Shun-Rong Zhang[1], Yukitoshi Nishimura[2], Philip J. Erickson[1], Ercha Aa[1], Hyosub Kil[3], Yue Deng[4], Evan G. Thomas[5], William Rideout[1], Anthea J. Coster[1], Robert Kerr[6], and Juha Vierinen[7]

[1]Haystack Observatory, Massachusetts Institute of Technology, Westford, MA, USA, [2]Center for Space Physics, Boston University, Boston, MA, USA, [3]Applied Physics Laboratory, Johns Hopkins University, Laurel, MD, USA, [4]Department of Physics, University of Texas at Arlington, Arlington, TX, USA, [5]Thayer School of Engineering, Dartmouth College, Hanover, NH, USA, [6]Computational Physics, Inc, North Chelmsford, MA, USA, [7]Department of Physics and Technology, The Arctic University of Norway, Tromsø, Norway

Abstract This study provides first storm time observations of the westward-propagating medium-scale traveling ionospheric disturbances (MSTIDs), particularly, associated with characteristic subauroral storm time features, storm-enhanced density (SED), subauroral polarization stream (SAPS), and enhanced thermospheric westward winds over the continental US. In the four recent (2017–2019) geomagnetic storm cases examined in this study (i.e., 2018-08-25/26, 2017-09-07/08, 2017-05-27/28, and 2016-02-02/03 with minimum SYM-H index −206, −146, −142, and −58 nT, respectively), MSTIDs were observed from dusk-to-midnight local times predominately during the intervals of interplanetary magnetic field (IMF) Bz stably southward. Multiple wavefronts of the TIDs were elongated NW-SE, 2°–3° longitude apart, and southwestward propagated at a range of zonal phase speeds between 100 and 300 m/s. These TIDs initiated in the northeastern US and intensified or developed in the central US with either the coincident SED structure (especially the SED basis region) or concurrent small electron density patches adjacent to the SED. Observations also indicate coincident intense storm time electric fields associated with the magnetosphere–ionosphere–thermosphere coupling electrodynamics at subauroral latitudes (such as SAPS) as well as enhanced thermospheric westward winds. We speculate that these electric fields trigger plasma instability (with large growth rates) and MSTIDs. These electrified MSTIDs propagated westward along with the background westward ion flow which resulted from the disturbance westward wind dynamo and/or SAPS.

Plain Language Summary Traveling ionospheric disturbances (TIDs) are an important means of storm time global dispersion of the solar wind and magnetosphere energy and momentum deposited at high latitudes. While the meridional propagation of large-scale TIDs is very efficient, zonal propagation is also very important. We provide the first observations of dramatic storm time zonal propagation of TIDs associated with strong subauroral dynamics and structures storm-enhanced density, subauroral polarization stream, and enhanced thermospheric westward winds. These are documented in a collection of Global Navigation Satellite System (GNSS) total electron content observations in the continental US during several recent geospace storms between 2016 and 2018. Medium-scale TIDs (MSTIDs) occurred predominately in the dusk-evening sector, propagating westward at up to 200 m/s phase speed. Thermospheric westward winds showed simultaneous enhancements, reaching up to 200 m/s. We suggest several magnetosphere–ionosphere–thermosphere coupling electrodynamical processes at subauroral latitudes trigger plasma instability and MSTIDs, and poleward electric fields induced by the disturbance wind dynamo facilitate the westward propagation of these electrified MSTIDs. These observations provide new scenarios for subauroral dynamic processes at the mesoscale level.

1. Introduction

Solar wind and magnetospheric energy, momentum, and mass injection into high latitudes are the origin of many ionospheric and thermospheric disturbances. Various heating processes in confined auroral regions excite atmospheric waves or traveling atmospheric disturbances (TADs) that can subsequently propagate globally (Francis, 1975; Hocke & Schlegel, 1996; Hunsucker, 1982; Lu et al., 2016; Richmond, 1978; Yeh & Liu, 1974; Zhang, 2021). The TAD propagation in the magnetic meridian plane is efficient where ions are set to motion by the oscillating neutrals. As a result, meridionally propagating traveling ionospheric disturbances (TIDs)

developed and to a large degree, these TIDs are manifestation of TADs. TADs lose some kinetic energy to the ions. The TAD and TID zonal propagations in the *F* region with a long periodicity (>the ion gyrofrequencies) are constrained strongly by the presence of magnetic field and the ions act as drag force on TADs (e.g., C. H. Liu & Yeh, 1969). Such constraints are eased if meridional polarization electric fields are embedded in TIDs to drive zonal plasma motion, or if the ion density is low, or if waves have short periodicities. Some of these electric fields embedded in TIDs have been recently confirmed at midlatitudes during quiet time postsunrise hours with significant TID zonal propagation for a few hours (Zhang, Erickson, Gasque, et al., 2021).

Storm time ionospheric electric fields are dynamic at middle and subauroral latitudes and sometimes are very intense at high and equatorial latitudes. Magnetosphere dawn-to-dusk electric fields, mapping to the ionosphere and creating convection cells poleward to auroral latitudes, can be significantly intensified and quickly expand or penetrate into low latitudes; solar wind and interplanetary electric fields (IEFs) can directly penetrate into the ionosphere (e.g., Huang, 2019; Jaggi & Wolf, 1973; Kelley et al., 1979; Nishida, 1968). These prompt penetration electric fields (PPEFs) have a zonal component to drive upward or downward ion drifts perpendicular to **B**. Therefore, they impact the intensity and location of equatorial ionization anomaly (EIA) and the development of equatorial plasma bubbles. The PPEF meridional component drives the zonal ion drift perpendicular to **B**, inducing important convection flow; in the dusk sector, this flow is in the opposite direction of Earth's counterclockwise (west-to-east) rotation. Subsequent shielding and overshielding can develop to cancel previously established PPEF and even create reversal electric fields at midlatitudes and low latitudes. The subauroral polarization stream (SAPS) electric field is poleward driving westward/sunward ion drift near the dusk sector (Foster & Burke, 2002). SAPS is an intense electric field within a narrow channel location near the midlatitude trough region as a result of storm time magnetospheric ring current dynamics coupling to the low conductivity ionosphere. Associated with the substantial ion flow, ion drag and frictional heating in the upper atmosphere lead to significantly elevated thermospheric westward winds (H. Wang et al., 2011) and subsequently impact meridional winds (Zhang et al., 2015), and also the likelihood of TAD/TID excitation and evolution (Guo et al., 2018) and other thermospheric variations (W. Wang et al., 2012). Additional electric fields can also arise due to dynamo action from the disturbanced neutral winds, with a large equatorward surge and a westward subrotation (Blanc & Richmond, 1980). This disturbance dynamo establishes the anti-Sq type current system which, at midlatitudes, has a poleward electric field component as well as a westward component during the day and an eastward component at night.

Storm time electric fields, along with other processes, are responsible for middle and subauroral latitude ionospheric perturbations during geomagnetic storms. For example, storm-enhanced density (SED) is a highly structured ionospheric electron density gradient at middle and subauroral latitudes. TEC elevation along a narrow channel is frequently observed with a base in the eastern US and extending across the continental US (CONUS) into the western Canada and Alaska. The SED plasma is convected sunward through the cusp into the polar cap, providing significant mass flux that fills the polar cap with high densities and forms the tongue of ionization. Before the Global Navigation Satellite System (GNSS) era, SED was considered an ionospheric positive phase effect at dusk during the early storm stage, called "dusk effect" (Buonsanto, 1999; Mendillo, 2006). The wide availability of GNSS data has considerably advanced our understanding through the TEC observation of SED spatial context and spatiotemporal evolution (Foster, 1993). Observations suggested a physical causal chain from SAPS flow to SED plume (Foster et al., 2007). But other factors potentially driving the SED morphology include the expansion or penetration of high-latitude electric fields mentioned earlier (Deng & Ridley, 2006; Heelis et al., 2009; J. Liu et al., 2016; Lu et al., 2020; Zou et al., 2014), the storm time expansion of the EIA crest to midlatitudes, equatorward surges of meridional winds, as well as other processes (see Foster et al., 2021; Zhang & Aa, 2021, and references therein).

In this study, we investigate the development of medium-scale traveling ionospheric disturbances (MSTIDs) during four geomagnetic storms using the GNSS TEC observations. The dense GNSS stations over CONUS allow us to resolve MSTID structures. We also use the coincident observations of SAPS and thermospheric neutral winds for the investigation of electric fields in MSTIDs. These events were on 2018-08-26 (year-month-day), 2017-09-07, 2017-05-28, and 2016-02-03 with minimum Dst index ranging from −206 to −53 nT. SAPS observations were available on 2017-09-07 with the Millstone Hill incoherent scatter radar (ISR) as well as with midlatitude Super Dual Auroral Radar Network (SuperDARN) line-of-sight (LOS) data for all the events, and thermospheric neutral winds were available for three of the events with the Millstone Hill High-Res Fabry–Perot

interferometer (FPI). The analysis of these results represents an initial attempt to understand effects of the storm time magnetosphere–ionosphere–thermosphere coupling and ionospheric electrodynamics on the zonally propagating MSTIDs.

2. Data and Method

Dramatic MSTIDs developed in the dusk–midnight sector during the geomagnetic disturbances main storm phase or near the beginning of storm recovery. Detailed solar wind magnetic/electric field and geomagnetic SYM-H data are shown in the following Section 3 for all individual cases (Figures 2, 5 and 7); here we provide brief remarks.

2.1. Event Overview

Case 1 during 2017-09-07/08 is characterized by a sharply intensified southward Bz, that is, a strong IEF enhancement in the Ey component. In addition to GNSS observations, the Millstone Hill ISR provided plasma drift measurements along with other plasma state parameters.

Case 2 during 2018-08-25/26 is characterized by a large SYM-H drop (−206 nT), the largest among the cases examined here. MSTIDs were identified during the sustained southward Bz period that started 6+ hr prior to the SYM-H minimum. In addition to GNSS observations, Millstone Hill High-Res FPI red-line (630 nm) data were available to provide thermospheric winds.

Case 3 during 2017-05-27/28 was a weaker geomagnetic storm, but still initiated strong MSTIDs in GNSS data at midlatitudes after 2 hr into the storm main phase when Bz was stably southward.

Case 4 during 2016-02-02/03 was a moderate geomagnetic storm with a minimum SYM-H −58 nT. MSTIDs in GNSS data were also observed with similar main features as in other cases. Both Cases 3 and 4 are additionally supported by the Millstone Hill FPI wind data.

2.2. GNSS, ISR, FPI, and Other Data

We analyzed GNSS TEC data to detect TIDs over the CONUS. GNSS processing algorithms that were used to produce TEC were developed at MIT Haystack Observatory (Rideout & Coster, 2006; Vierinen et al., 2016). The same data source and TID detection were used recently in TID studies to understand effects of the solar eclipse, solar flare, geomagnetic storms and substorms, trans-polar dynamics, subauroral dynamics, lower atmospheric coupling, etc. (e.g., Aa et al., 2021; A. J. Coster et al., 2017; England et al., 2021; Jonah et al., 2018; Lyons et al., 2019, 2021; Nishimura et al., 2020; Sheng et al., 2020; Zhang, Coster, et al., 2019; Zhang, Erickson, et al., 2019; Zhang et al., 2017, 2022).

In order to detect TIDs, we calculated differential TEC using an approach that removes the smooth background ionospheric variations. Such background variations are determined by a low-pass filtering procedure using the Savitzky–Golay filter (Savitzky & Golay, 1964). The filter algorithm uses a convolution process with least squares fitting of successive subsets of windows of a given length (e.g., 30 or 15 min) involving time-adjacent TEC data points from the same GNSS satellite–receiver pair and a linear basis function set. Since we are interested in MSTIDs, this study used a 15 min window to minimize influences of large-scale TIDs (LSTIDs) and also of large TEC gradients associated with SED plume or midlatitude main trough. A 30 min window was used for the faint disturbance event Case 4. These strategies appear very successful as demonstrated in the distinct differences between the calculated ΔTEC and the original TEC in the result sections. A 25° cutoff elevation for receiver–satellite raypaths was used to eliminate data close to the horizon. Data at the start and the end of each continuous segment from the same GNSS satellite–receiver pair were disregarded to avoid potential "edge" effects (Zhang, Coster, et al., 2019; Zhang, Erickson, Vierinen, et al., 2021). Similar differential TEC analysis methods have been explored extensively since the work of A. Saito et al. (1998), with some revisions for real-time applications (e.g., Belehaki et al., 2020). The accuracy of this method is based on the accuracy of the GNSS phase measurement, which is less than 0.03 TEC units (A. Coster et al., 2012), as all satellite and receiver bias terms cancel out in a differential sense. Figure 1 demonstrates TID detection from GNSS TEC data for four receiver–satellite pairs

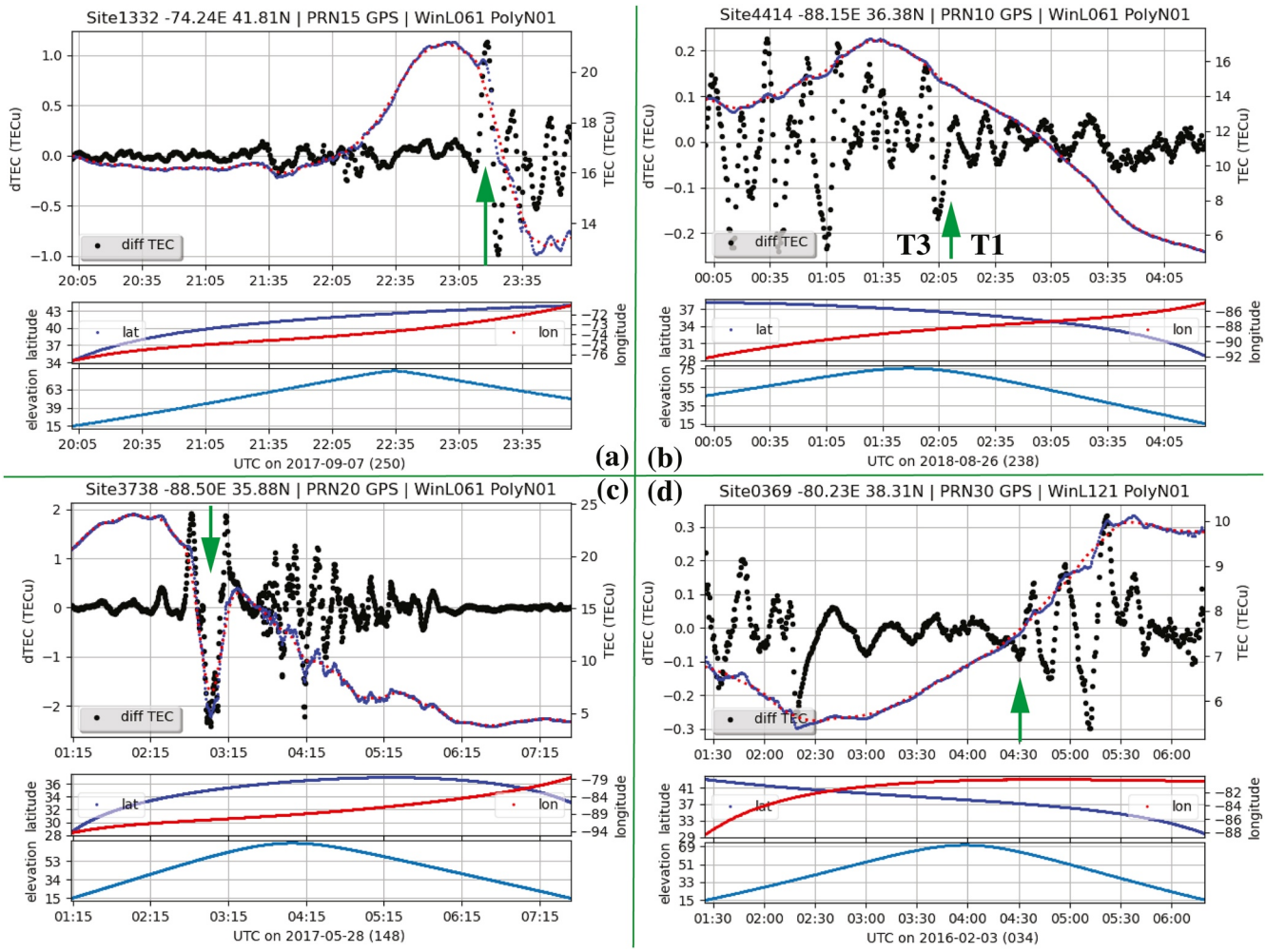

Figure 1. Demonstration of traveling ionospheric disturbance (TID) detection from Global Navigation Satellite System (GNSS) TEC observations for Case 1 (a), Case 2 (b), Case 3 (c), and Case 4 (d). In the top frame of each case panel shows TEC from a receiver and satellite pair (blue), background trend (red), and detrended differential TEC (black). Ionospheric pierce location and satellite elevation are in the other two frames. Notice that Case 4 used a 30-min sliding window, whereas other cases used 15-min. T1 and T3 in (b) correspond to those in Figure 6. The green arrow marks a specific characteristic time associated with the TID morphological change as detailed in the text.

corresponding to the four cases of interest in this work. Some of the characteristic variations in this figure will be further examined in the next section.

This study also utilized eastward ion drift data at ~300 km altitude as derived from the ISR observation at Millstone Hill (42.6°N, 71.5°W). This same data set was described in Zhang, Erickson, et al. (2019). Thermospheric winds in the *F* region were also measured for Cases 2–4 by the colocated FPI using the Doppler shift of the red-line 630 nm airglow emission. Detailed technical descriptions of the FPI system are provided along with the data in the Madrigal database (http://openmadrigal.org) and by Kerr (2019); Zhang et al. (2015) provided a brief version where local wind components are determined based on the LOS neutral motion measurements in zonal (east and west) and meridional (north and south) directions with 45° elevation. In this study, we present only the original LOS data in the four directions to preserve important spatial variations in the wind data (Emmert et al., 2003). Particularly, the horizontal spatial separation of E-W or N-S emission layers at 630 nm (i.e., ~250 km) is ~500 km.

To supplement the ion drift data from the Millstone Hill ISR, we present observations from five midlatitude SuperDARN radars: Blackstone (BKS, 37.10°N, 77.95°W), Fort Hays East and West (FHE and FHW, 38.86°N, 99.39°W), and Christmas Valley East and West (CVE and CVW, 43.27°N, 120.36°W). SuperDARN radars

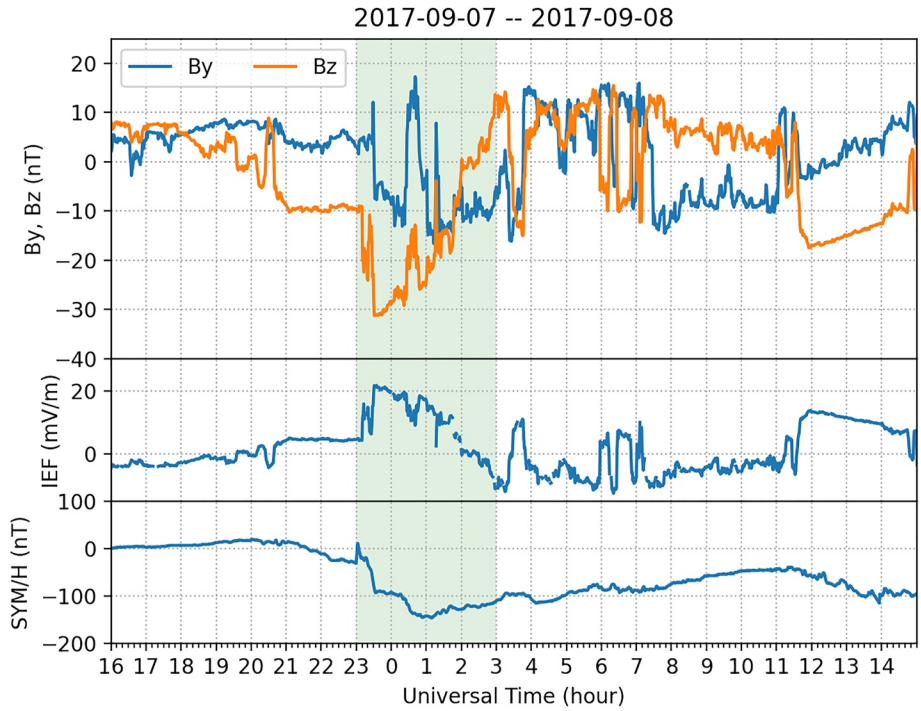

Figure 2. Solar and geomagnetic conditions during 2017-09-07/08, 2017 (Case 1). From top to bottom panels are interplanetary magnetic field components in By and Bz, interplanetary electric field components Ey, and SYM-H index. The light-green shaded area is when medium-scale traveling ionospheric disturbances (MSTIDs) were observed in the continental US as shown in the following two figures.

measure the LOS Doppler velocity of backscattered high-frequency (HF) radio signals from field-aligned, decameter-scale plasma irregularities at *E* and *F* region altitudes (Chisham et al., 2007; Greenwald et al., 1995; Nishitani et al., 2019). Note that observations were not available from the FHE or FHW radars during Cases 2 and 4.

We examined also ionosonde observations at Millstone Hill, Wallops Island (37.8°N, 75.5°W), and Eglin AFB (30.5°N, 273.5°W). They are located in the eastern US at midlatitudes where MSTIDs, SED, or SAPS features are identified. We browsed ionograms to find out the Es-layer information. These ionograms were taken with typically 5–15 min intervals.

3. Result and Analysis

We present the observational results during the four storms as follows: we start with a description of solar wind and geomagnetic conditions, then present MSTIDs at subauroral/midlatitudes and their corresponding TEC maps, and finally demonstrate the zonal propagation in keograms along with time variations of ionospheric zonal drifts or thermospheric zonal winds. We also provide (as supplementary) animations of dTEC maps at the 1-min cadence for all the events to demonstrate the dramatic propagation and evolution of MSTIDs.

3.1. Case 1 (2017-09-07/08)

This geospace storm started with Bz oscillations before being stably southward between 21:00 and 23:00 UT on 2017-09-07 and subsequently sudden intensification at 23:00 UT (Figure 2). This latter excursion took 3 hr and ended with Bz returning northward at 02:00 UT on the following day. Corresponding IEF Ey is suddenly elevated. During this 3-hr period between 23:00 and 02:00 UT, GNSS TEC exhibited dramatic changes with SED plumes, equatorward-propagating LSTIDs passing through the CONUS (Zhang, Erickson, et al., 2019), and MSTIDs. Shown in Figure 3 are those MSTIDs (marked as T1) in the differential TEC data on the left column and the corresponding TEC with SED plume on the right column. Notice that those MSTIDs reported in Zhang,

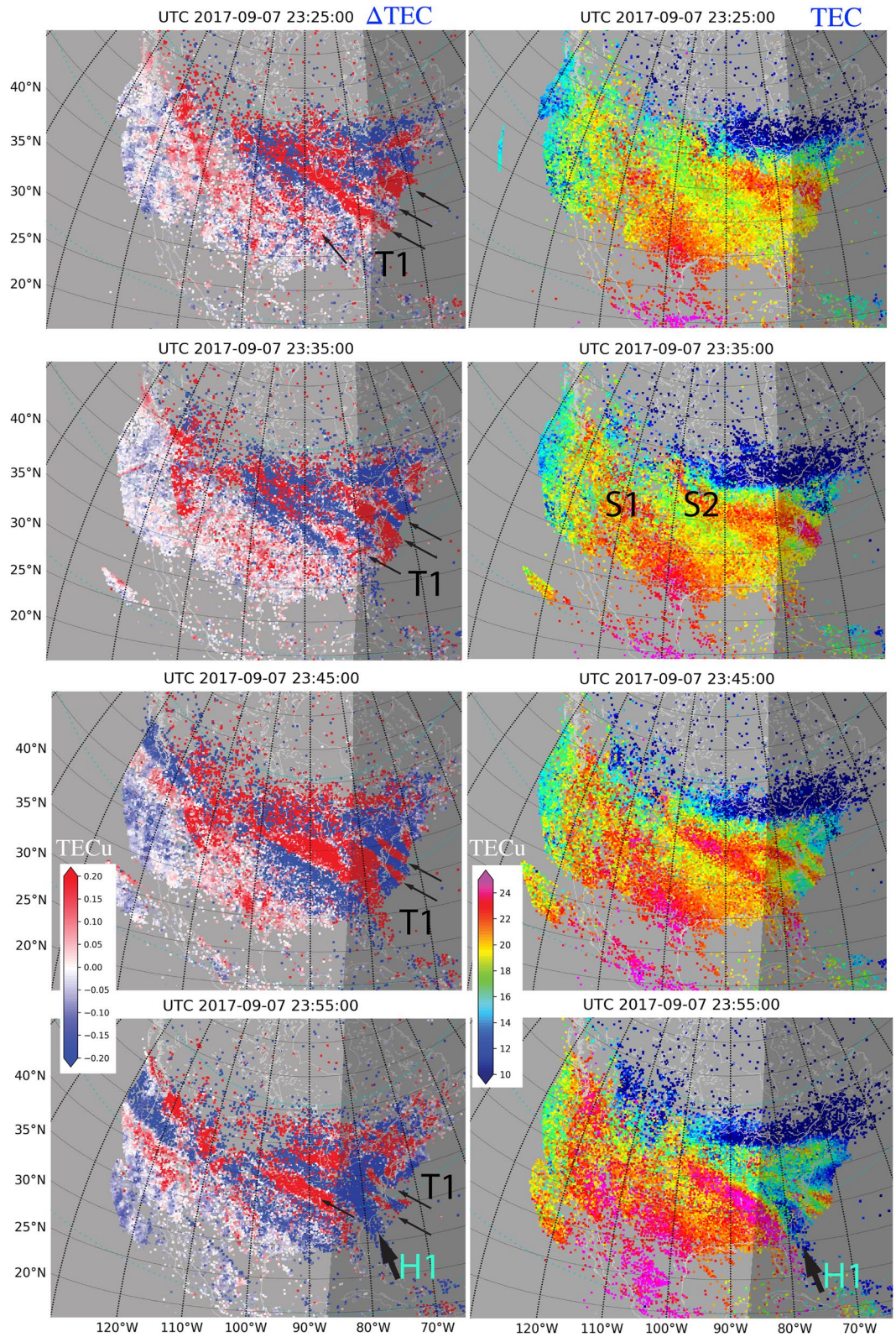

Figure 3. Characteristic maps of Global Navigation Satellite System (GNSS) TEC (right column) and corresponding differential TEC (left column) at four 10-min interval instances for Case 1 during 2017-09-07/08. Some clear traveling ionospheric disturbance (TID) wavefronts apparently parallel to each other are marked as T1. TEC enhancement structures of interest are marked as S1 and S2; a large TEC depletion structure is marked as H1.

Erickson, et al. (2019) for the same period have larger scales because of using a 30-min detrending window as compared to the 15-min window in the present study. These MSTIDs have wavefronts elongated along the NW-SE direction. They are zonally separated by 2°–5° longitude (200–500 km) and propagated southwestward.

These MSTID wavefronts exhibited certain overlapping in space and time with the SED structure and other TEC enhancement structures (marked as S1 and S2 for 23:35 UT), although the 15-min window detrending has effectively removed structures with large TEC gradients, leaving well-organized MSTIDs in dTEC data. The S1 TEC structure is larger in size with a clear base in the south and may be identified as a SED with both a long plume and a TEC-elevated base; S2 is a smaller TEC substructure separated from the S1 SED but has additional branches. The MSTIDs are hosted predominately by S2. A large depletion marked as S3 for 23:55 UT is collocated with the bubble-like ionospheric superdepletion structure identified by Aa et al. (2019).

The temporal evolution and zonal propagation of MSTIDs are better illustrated in keograms as shown in the left column of Figure 4. The vertical strips indicate the near simultaneous disturbance along all relevant longitudes and its successive presence, most likely caused by the equatorward propagating LSTIDs with zonal wavefronts. The MSTID signatures can be identified at 32°–40°N latitudes, most significantly at the southern latitudes of 32°N on the nightside near the dusk terminator. These MSTIDs propagated westward as marked by arrows at a speed (230 m/s) close to or slower than the terminator speed (~400 m/s). The most active period of MSTIDs was between 23:00 and 03:00 UT as also light-green shaded area in Figure 2 when IEF Ey was substantially elevated during the main phase and the early recovery phase of the storm.

The sudden appearance of MSTIDs in these midlatitude regions was close to 65°–75°W almost right at ~23:00 UT. Figure 1a shows clearly the dTEC disturbance onset at ~23:15 UT (green arrow) and subsequently large fluctuations. The preonset fluctuations were also observed starting at ~21:00 UT when Bz turned southward (Figure 2). This ~23:15 UT onset was close to the start time of significantly elevated IMF Ey and dramatic *F*2 region westward ion velocity enhancements peaking at 2 km/s (Figure 4(1d)), as measured by the Millstone Hill ISR for 45°N (slightly northward of the radar). The SAPS was measured in the proximity of Millstone Hill radar as well as to the west of the site as shown in the SuperDARN LOS velocity data (Figure 12a). However, the MSTIDs appeared in broad latitudes including Millstone Hill as well as at least 10° equatorward in latitude. Both the SAPS drift and MSTID zonal propagation were westward near dusk; however, MSTID propagation was much slower. The SAPS duration at Millstone Hill was brief (<1 hr), but the MSTIDs equatorward propagation at Millstone Hill was active 1–3 hr beyond the SAPS time.

3.2. Case 2 (2018-08-25/26)

The Case 2 event developed during the sustained large southward IMF Bz for nearly 16 hr between 2018-08-25 and 2018-08-26. During this period, IEF Ey was stably positive (dawn to dusk), and SYM-H reached a minimum of −206 nT, the strongest among the four cases (Figure 5).

During this intense geospace disturbance period, the SED plume formed over the CONUS at the storm main phase (Figure 6). By 00:30 UT on the 26th, the SED plumes near the dusk showed a characteristic base in the northeastern US which was on the nightside, and the plume was on the dayside elongated in the northwest-southeast direction. As the midlatitude ionospheric trough moved into the northeastern US on the night side, TEC in the SED base region remained elevated but the TEC magnitude within the plume decreased. The SED base and plume gradually moved westward but slightly behind the solar terminator (i.e., on the nightside). By 04:00 UT, the SED base and plume were visible only on the US west coast, whereas the east coast saw the midlatitude trough as well as the extended TEC depletion further equatorward of it.

Dramatic TID activities were observed (see left panels in Figure 6) during the SED plume presence. The zonal alignment of wavefronts are LSTIDs (even though the differential TEC was derived from 15-min window detrending, they remain visible). The MSTIDs marked as T1 with multiple fronts occurred on the nightside near the US east coast and were intensified in amplitude further to the west at 02:30 UT and later. They were elongated NW-SE and separated by 2°–3° in longitude. The T3 structure elongated NE-SW (rather than NW-SE as for the T1 structure) was observed in the southern US on the dayside and rotated counterclockwise to be approximately along the terminator near dusk. Unlike T1, T3 appears to be initiated in the US south. The T1 and T3 differences can also be seen in the original differential TEC data in Figure 1b (separated by the green arrow). At 00:30 UT,

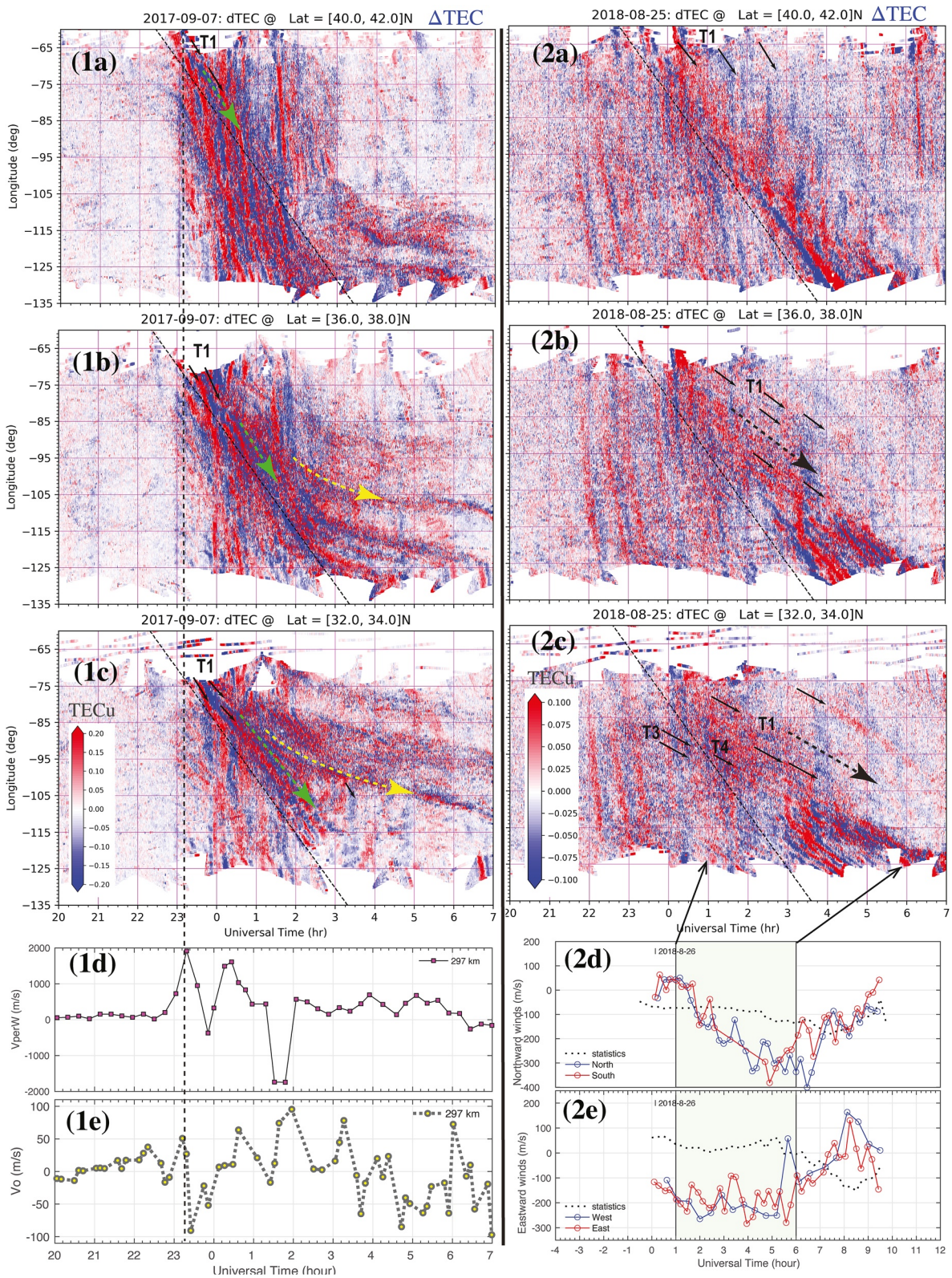

Figure 4. Traveling ionospheric disturbance (TID) zonal propagation for Case 1 (left) and Case 2 (right) at three latitudes: (1a, 2a) 40°N, (1b, 2b) 36°N and (1c, 2c) 32°N. Short black arrows marked as T1, T3, and T4 correspond approximately wavefronts in Figures 3 and 6. Long green, yellow, and black arrows represent the primary TID propagation directions. Additional panels (1d) and (1e) show Millstone Hill incoherent scatter radar measurements of the *F*2 region eastward ion drifts and vertical ion drift V_0, and panels (2d) and (2e) show Millstone Hill FPI red-line poleward and eastward winds.

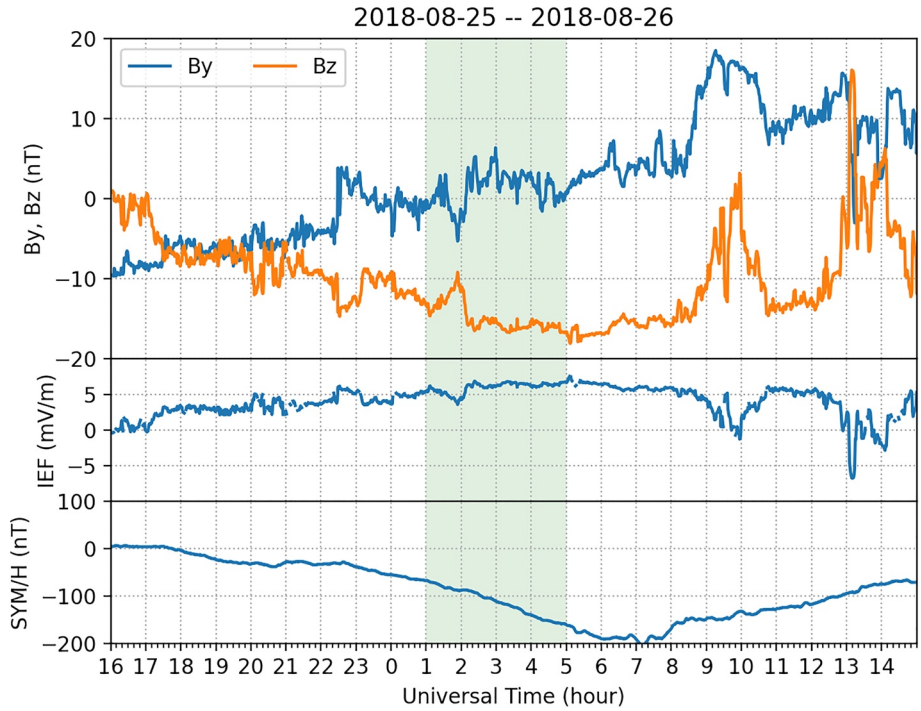

Figure 5. Solar and geomagnetic conditions during 2018-08-25/26, 2017 (Case 2). From top to bottom panels are interplanetary magnetic field components in By and Bz, interplanetary electric field components Ey, and SYM-H index. The shaded area is when medium-scale traveling ionospheric disturbances (MSTIDs) were observed in the continental US.

the periodic small patches (marked as T2) near 50°N geographic latitude separated by ∼5° in longitude were moving westward at a speed much slower than the SAPS ion drift. This storm time auroral/subauroral phenomenon, also present in other cases, deserves dedicated future studies.

The spatial–temporal evolution of the MSTIDs as shown in the keograms in the right column of Figure 4 exhibited clear westward propagation at subrotational speed of the earth at 190 m/s. They were most pronounced in the south of Millstone Hill between 01:00 and 06:00 UT on 2018-08-26. This time period saw dynamical thermospheric wind disturbances. Figures 4(2d) and 4(2e) are the Millstone Hill FPI equatorward and eastward winds during this night as well as corresponding 30-day averages centering on this night. These wind data indicated the equatorward wind surge with 300 m/s maximum speed around 05:00–06:00 UT (or 00:00–01:00 LT) was likely caused by auroral heating. The westward wind surge by ∼200 m/s was even more dramatic for more than ∼5 hr between 01:00 and 06:00 UT. The onset of this westward wind surge seems to advance the equatorward winds by hours, although the exact surge onset could not be determined. This westward wind variation is similar to those identified as a SAPS effect causing large ion drag forcing in H. Wang et al. (2011), W. Wang et al. (2012), Zhang et al. (2015), Ferdousi et al. (2019), and Aa et al. (2021). Evidence of SAPS presence can be seen in Figure 12b from the HF backscatter echoes to the west of Millstone Hill, adjacent to the major areas of active MSTIDs in the southeast. We note here the westward wind velocity is comparable to the MSTID westward propagation velocity.

3.3. Case 3 (2017-05-27/28)

Case 3 was during a stable IMF Bz southward period on 2017-05-27/28 (Figure 7). Sudden IEF Ey enhancement started at 22:00 UT with a sudden Bz southward turning. SYM-H minimum reached −142 nT. Therefore the disturbance in this period was less intense as in Cases 1 and 2, but Cases 3 and 2 were both in summer of Northern Hemisphere.

The SED structure developed (Figure 8) following the abrupt Bz southward turning at 22:00 UT. Three hours later, the area of the SED base (i.e., the southern end of the plume) became substantial at 01:00 UT and covered over the central US, not too far from the dusk terminator. SAPS echoes were found primarily to the north of

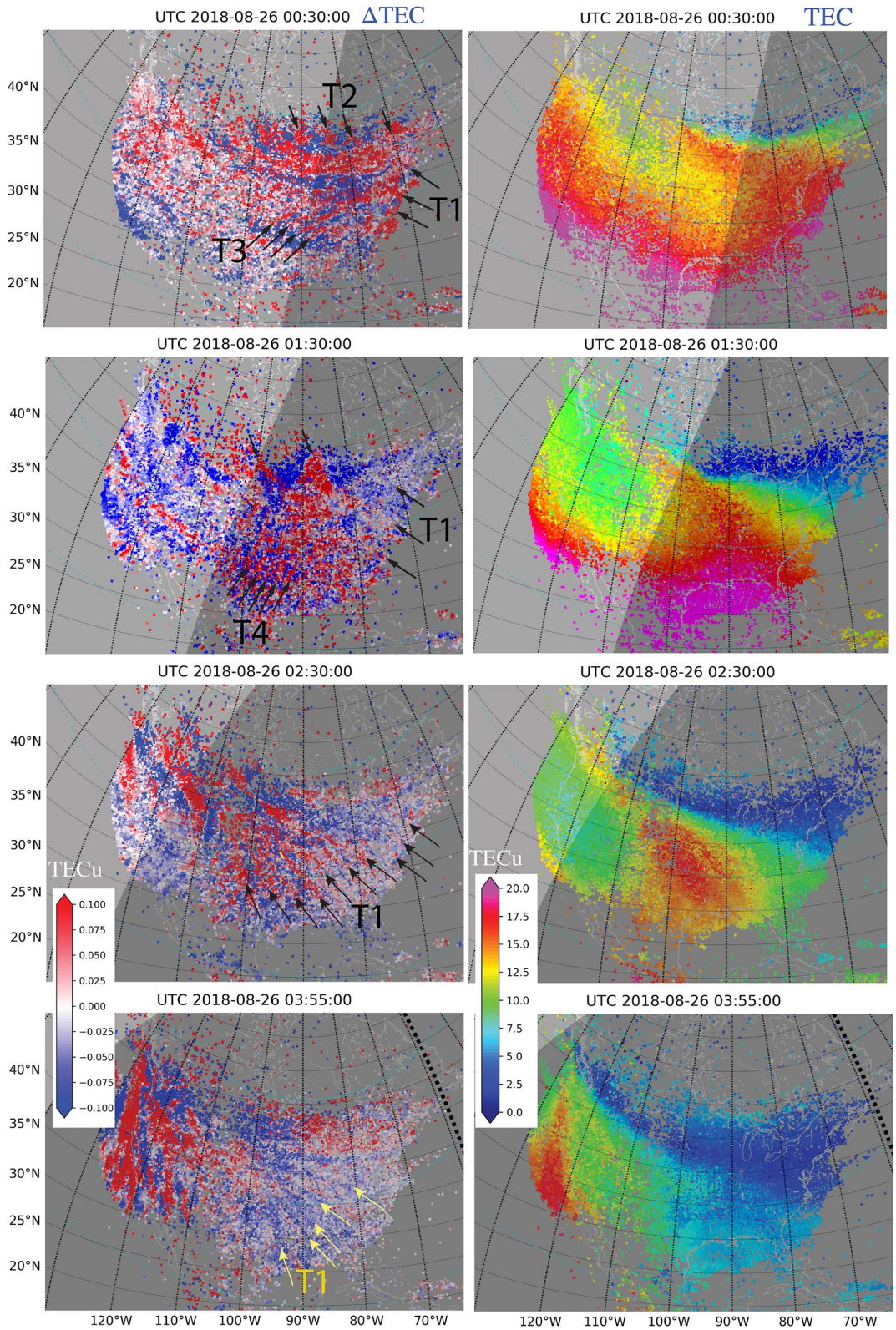

Figure 6. Characteristic maps of Global Navigation Satellite System (GNSS) TEC (right column) and corresponding differential TEC (left column) at four instances for Case 2 during 2018-08-26. Some clear traveling ionospheric disturbance (TID) wavefronts apparently parallel to each other are marked as either T1, T2, T3, or T4.

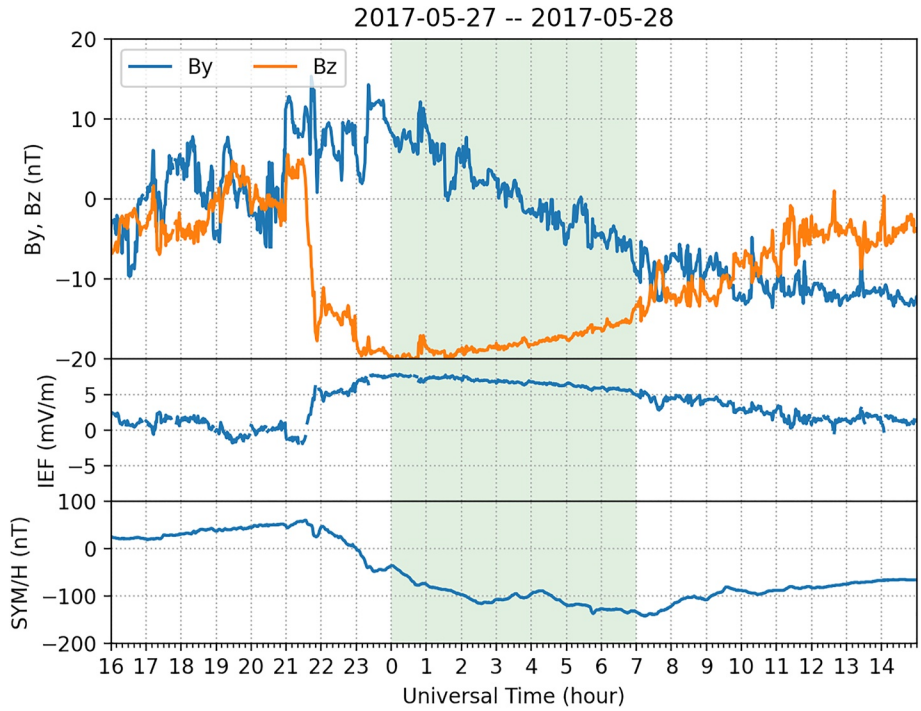

Figure 7. Solar and geomagnetic conditions during 2017-05-27/28 (Case 3). From top to bottom panels are interplanetary magnetic field components in By and Bz, interplanetary electric field components Ey, and SYM-H index. The shaded area is when medium-scale traveling ionospheric disturbances (MSTIDs) were observed in the continental US.

the plume (Figure 12c). Inside the SED at ~50°N latitude, the multiple periodical patches marked as T1 on the dayside were present, similar to Case 2. The MSTIDs which initially developed in the northeast US on the nightside expanded westward as the terminator swept westward. Multiple fronts separated by 2°–3° in longitude were elongated NW-SE, similar to those in Cases 1 and 2. LSTIDs with long wavefronts aligned in the zonal direction were concurrent and adjacent to these MSTIDs. During the TID evolution, the SED base was moving/corotating westward and electron density structures toward the midnight sector (to the east side of the SED, marked as S1 and S2) appeared to have detached from the SED or formed independently from the SED. These structures and MSTIDs coexisted. Figure 1c shows also the TEC hole (near the green arrow), corresponding to the density depletion at 03:10 UT adjacent to S1 on the TEC maps (Figure 8), and the subsequent (eastside) MSTIDs.

The onset of these westward-propagating MSTIDs were at ~00:30 UT during the time when SAPS was active (Figure 12c), and they remained sufficiently visible until at least 07:00 UT. They propagated westward at a speed of ~200 m/s (Figure 9). The MSTIDs propagated through Millstone Hill between 70° and 75°W longitudes at 02:00 UT. At this moment, the Millstone Hill FPI also measured thermospheric winds in both east and west directions at 45° elevation. The airglow emission locations might be 70°W for the east beam and 75°W for the west beam. Figure 9(3e) indicates 200 m/s eastward winds at 70°W and −200 m/s westward 75°W. Note these FPI data are considered as being good quality. This wind observation suggests a large wind shear in the zonal direction when MSTIDs were growing near Millstone Hill (Figure 9(3a)). Corresponding to the MSTID westward propagation at 200 m/s, the winds on the west of Millstone Hill were apparently strongly westward at a similar speed before 03:00 UT. No more MSTID passage was observed after 03:00 UT as the zonal wind returned to nominal speeds.

3.4. Case 4 (2016-02-02/03)

Case 4 during 2016-02-02/03 had a stable IMF Bz being southward and IEF Ey down-to-dusk for 7 hr (22:00–05:00 UT; Figure 10). The SYM-H reached a minimum at merely −58 nT. This was a winter case with minor geomagnetic disturbances.

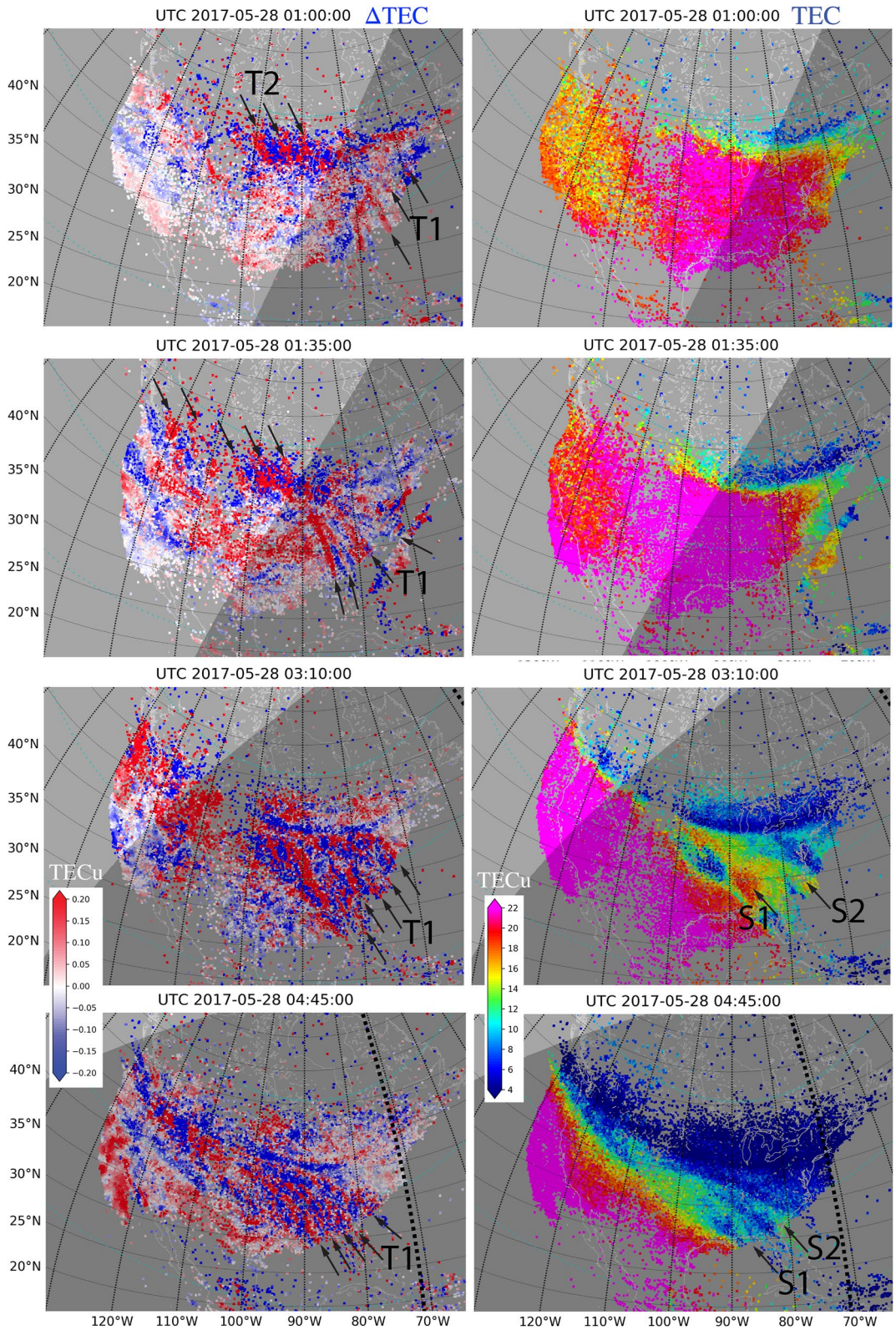

Figure 8. Characteristic maps of Global Navigation Satellite System (GNSS) TEC (right column) and corresponding differential TEC (left column) at four instances for Case 3 during 2017-05-27/28. Some clear traveling ionospheric disturbance (TID) wavefronts apparently parallel to each other are marked as either T1 or T2. TEC enhancement structures are marked as S1 or S2.

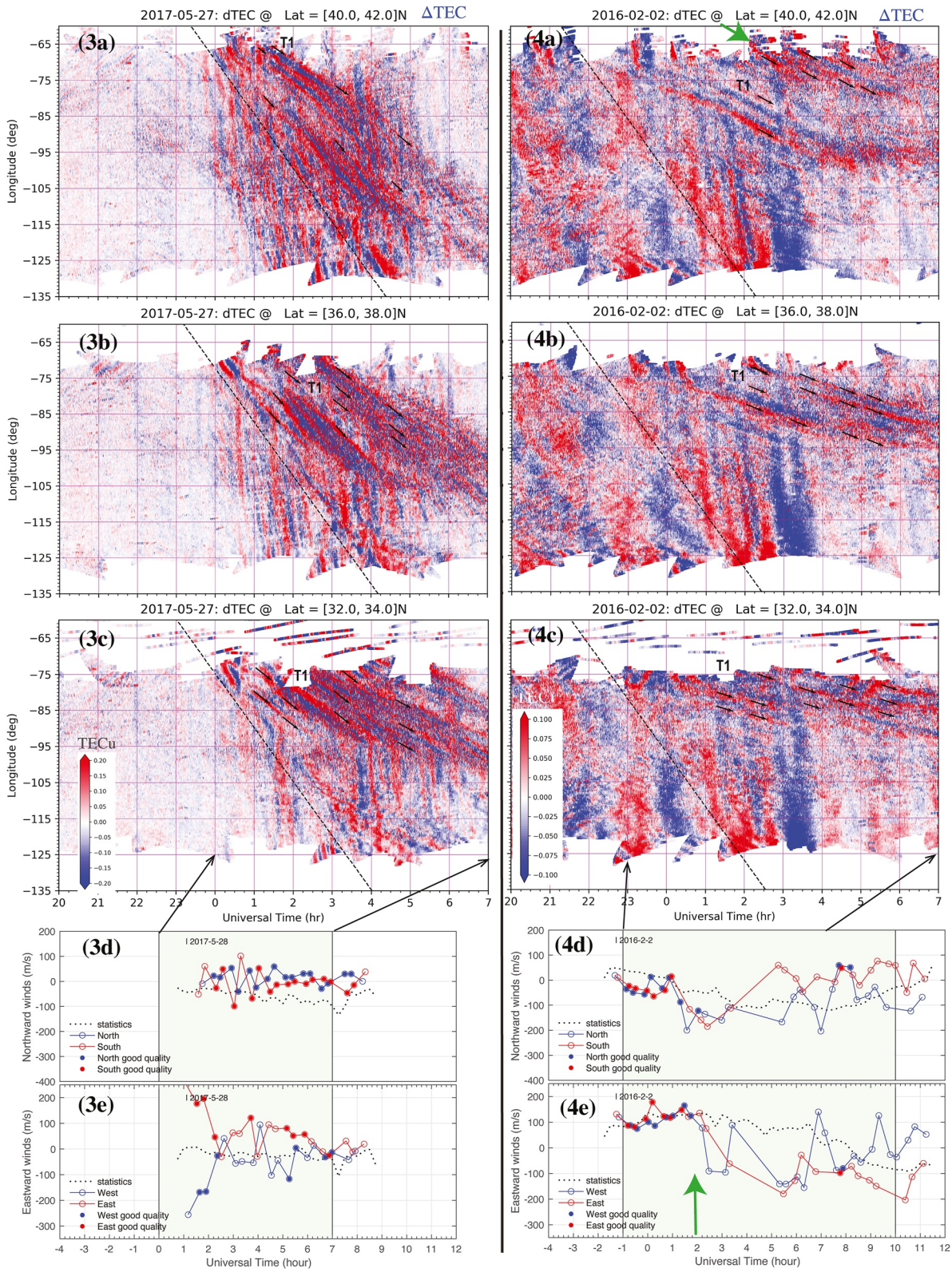

Figure 9. Traveling ionospheric disturbance (TID) zonal propagation for Case 3 (left) and Case (4) at three latitudes: (3a, 4a) 40°N, (3b, 4b) 36°N, and (3c, 4c) 32°N. Short black arrows marked as T1 correspond approximately wavefronts in Figures 8 and 11. Additional panels (3d) and (4d) show Millstone Hill FPI red-line winds. The full dots are data with good quality (quality flag 0) where bad points were filtered out, and the circle dots are data slightly worse (quality flag 1) but better than the lowest quality data (flag 2). The reduced quality was caused by aurora (e.g.), slight contamination, or just bright twilight as noted in the data document.

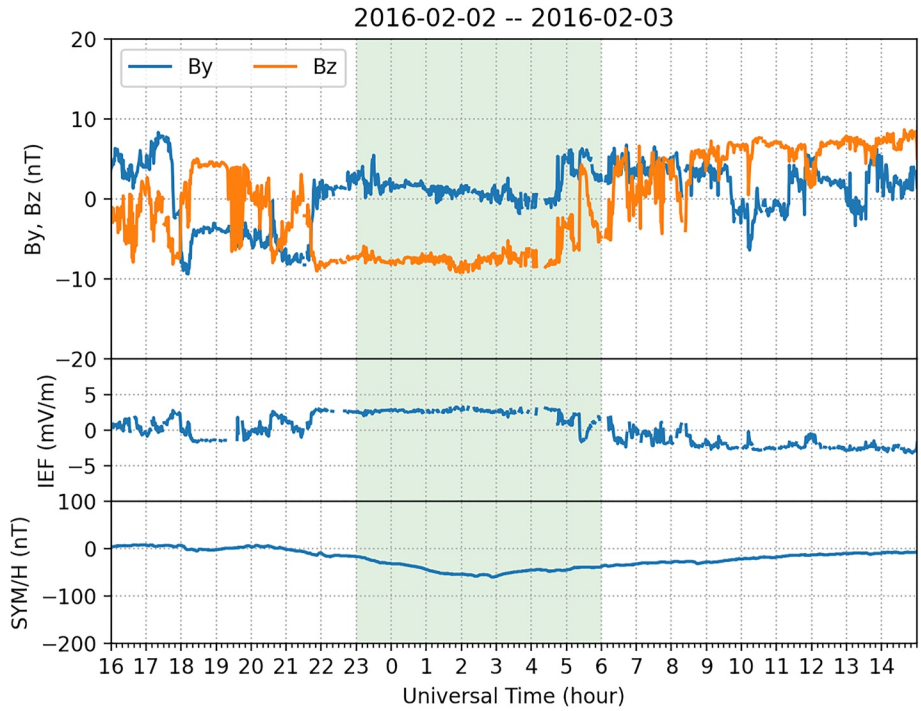

Figure 10. Solar and geomagnetic conditions during 2016-02-02/03 (Case 4). From top to bottom panels are interplanetary magnetic field components in By and Bz, interplanetary electric field components Ey, and SYM-H index. The shaded area is when medium-scale traveling ionospheric disturbances (MSTIDs) were observed in the continental US.

The MSTIDs started to occur on the nightside at the start of storm recovery phase in the region where the midlatitude ionospheric trough has extended into (Figure 11). Electron density bands marked as S1 and S2 in the TEC maps were aligned in the NW-SE direction in this region. MSTIDs marked as T1 clearly overlapped with these TEC structures but MSTIDs were much more organized structures. Similar to previously shown cases, SAPS echoes can be seen in the northwest adjacent to MSTIDs (Figure 12d). The MSTID wavefronts were NW-SE and they were initiated in the northeastern US but evolved southwestward. These MSTIDs were located very close to the midnight sector. The MSTID intensification at 04:45 UT and later in these maps can be seen in the original differential TEC data shown in Figure 1d.

The westward propagation of these MSTIDs is best demonstrated in the longitude-UT keograms for a few latitude bins (Figure 9). Over the 6-hr time span at night for a given location, multiple MSTIDs passed over gradually at 70–100 m/s phase speed. The speeds decreased as the waves arrived in the central US. Some intensification at Millstone Hill can be seen starting at 02:00 UT (the green arrow in the top panel) with high wave amplitudes. This appears coincident with the elevated westward neutral wind at Millstone Hill (Figure 9(4e)). The zonal wind speed was at ∼100 m/s.

4. Discussion

The observation results described in the previous section indicate that those MSTIDs at midlatitudes were in the nighttime sector (dusk to midnight) and coincident with storm-related features during the intervals of stably southward IMF Bz. Multiple wavefronts were 2°–3° longitude apart, elongated predominately NW-SE, and propagated westward at a range of phase speed between 100 and 300 m/s. They were normally originated in the northeastern US and as they propagated into the central US, they were either intensified or well organized. They were concurrent with the SED structure (especially the SED base region) or with other smaller electron density patches lagged behind (i.e., to the east of) the SED. The onset of the MSTIDs appeared to accompany with a SAPS or almost synchronized with the elevated westward thermospheric winds.

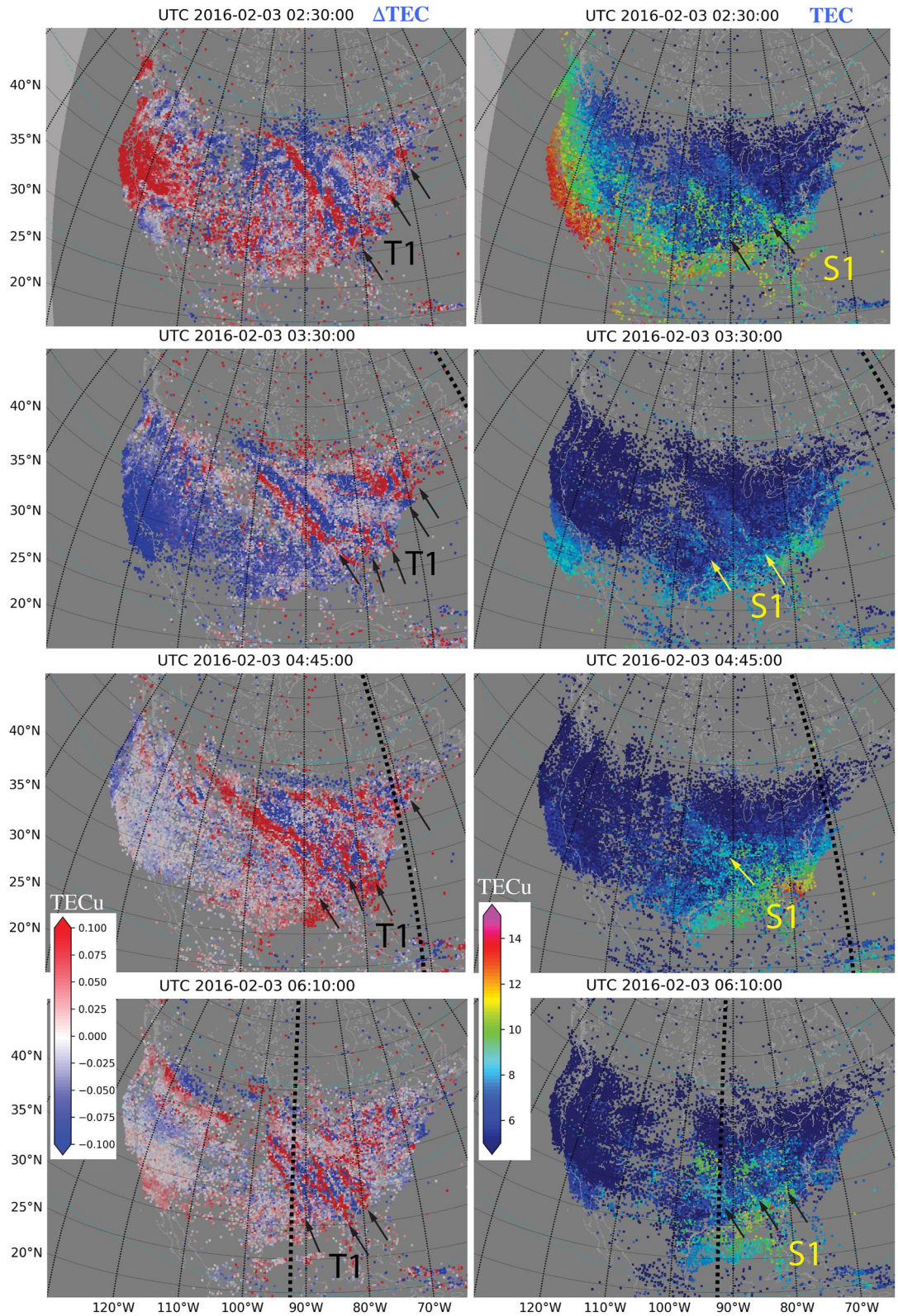

Figure 11. Global Navigation Satellite System (GNSS) TEC maps (right column) and corresponding differential TEC maps (left column) at four instances for Case 4 during 2016-02-03. Note: since the disturbances are relatively weak, we have used (only in this case) a 30-min sliding window for detrending in order to detect larger waves. Some clear traveling ionospheric disturbance (TID) wavefronts apparently parallel to each other are marked as T1. TEC enhancement structures are marked as S1.

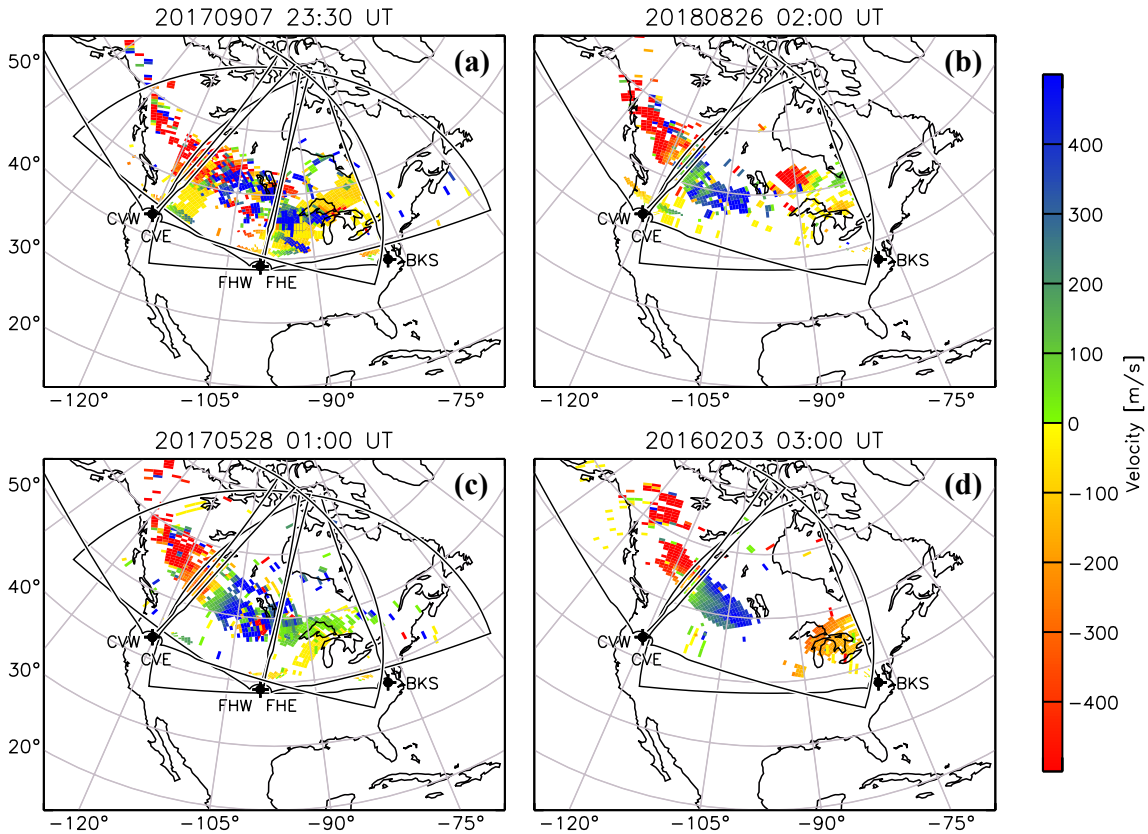

Figure 12. Line-of-sight (LOS) velocity measurements from the Blackstone (BKS), Fort Hays East (FHE), Fort Hays West (FHW), Christmas Valley East (CVE), and Christmas Valley West (CVW) midlatitude Super Dual Auroral Radar Network (SuperDARN) radars corresponding to (a) Case 1 (2017-09-07/08), (b) Case 2 (2018-08-25/26), (c) Case 3 (2017-05-27/28), and (d) Case 4 (2016-02-02/03). Positive (green-blue) and negative (yellow-red) LOS velocities indicate plasma motion toward or away from each radar, consistent with a westward subauroral polarization stream (SAPS) channel over North America during each event.

Some of the above-mentioned features are consistent with nonstorm midlatitude MSTIDs at night (e.g., Kil & Paxton, 2017; Kotake et al., 2007; Martinis et al., 2011; Otsuka et al., 2004, 2013; S. Saito et al., 2007; Shiokawa, 2003; Shiokawa et al., 2002; Tsugawa et al., 2007; Valladares & Sheehan, 2016), especially, in terms of timing and the electrified wavefront orientation and propagation. Those ionospheric waves have been ascribed to the effect of Perkins instability (e.g., Kelley, 2011; Makela & Otsuka, 2011; Perkins, 1973; Yokoyama, 2013; Zhou & Mathews, 2006). The external effective (DC) electric field $\mathbf{E}_0^*$, when being applied to the wavy electron density fluctuations, will induce polarization electric fields in order to maintain the current continuity across the wavefronts with inhomogeneous Pedersen conductivity. If $\mathbf{E}_0^*$ direction is northeastward in the northern hemisphere, these electric fields generate upward ion drifts for lower conductivity regions. The net ion velocity established by these vertical drifts and the downward velocities caused by the gravity-induced diffusion will grow as a function of height, causing the unstable low-density zone by transporting lower density plasma at low altitudes to high altitudes. This Perkins instability has a growth rate $\gamma = \sin(\theta - \alpha)\sin\alpha\cos D \ \ \mathrm{E}_0^*/(\mathrm{BH})$ where θ and α are the angles between $\mathbf{E}_0^*$ and the geographic eastward and between the electron density wave vector and the geographic eastward, respectively, D is the geomagnetic dip angle, B geomagnetic field intensity, and H the neutral scale height. The effective electric field is defined as $\mathbf{E}_0^* = \mathbf{E}_0 + \mathbf{U} \times \mathbf{B}$ where E is the external electric field, often associated with the F region dynamo during quiet times, and $\mathbf{U}$ is meridional winds. This growth rate may be very small, given the velocity $\mathbf{E}_0^*/\mathbf{B} = \mathbf{E}_0/\mathbf{B} + \mathbf{U} \times \mathbf{B}/\mathrm{B}$ is often smaller than 100 m/s at midlatitudes. Additional electrical fields such as those associated with the Es instability may be large enough to produce visible MSTIDs via the Perkins instability (e.g., Cosgrove & Tsunoda, 2004; Duly et al., 2014; Narayanan et al., 2018; Yokoyama et al., 2009).

Ionosonde observations (not shown here) at Millstone Hill, Wallops Island (37.8°N, 75.5°W), and Eglin AFB (30.5°N, 273.5°W) indicated that the MSTIDs events reported here in TEC observations were largely Es-layer

irrelevant. MSTIDs were above Eglin AFB for all the cases, however, no Es-layer occurred during the intervals of Cases 1–3 MSTIDs, and for Case 4 only a weak Es-layer (with foEs < 3 MHz) occurred briefly (03:00–04:00 UT). Case 2 MSTID interval had no Es-layer at Wallops Island and moderately active Es-layers after 03:15 UT at Millstone Hill which, however, was far from the main MSTID region; for Cases 1, 3, and 4 MSTID intervals, no Es-layers were observed at Millstone Hill (no ionosonde data were available at Wallops Island).

During geospace storms, several intensified electric fields, as described in Section 1, can be very significant and provide large Perkins instability growth rates. Zhang, Erickson, et al. (2019) suggested that the poleward SAPS electric fields, which drove 2 km/s ion drifts in Case 1, are sufficient to induce Perkins instability with a large growth rate. Indeed the SAPS electric field contributes to $\mathbf{E}_0$ and is likely a factor of 20–50 of other terms in $\mathbf{E}_0$. As LSTID wavefronts enter into the SAPS channel or its vicinity where the westward ion drift near dusk is significant, the westward neutral wind enhancement and frictional heating to neutrals and ions, both processes being associated with SAPS, as well as large electron density gradients such as SED, can all modify the thermospheric and ionospheric conditions for LSTID propagation and likely cause some rotation of LSTID wavefronts from zonal to meridional; Figure 4(1e) shows fluctuations of the *F*2-region vertical ion drift. The peak-to-peak vertical ion drift change is substantial, reaching 150 m/s near the SAPS peak. Moderate to intense SAPS signatures were observed by the midlatitude SuperDARN radars for several hours during all these different levels of geomagnetic disturbance cases, with LOS velocities exceeding 500 m/s; they were located northwest adjacent to MSTIDs which were initially in the southeast. Therefore, supported by the large SAPS electric field, Perkins instability over the rotated wavefronts can quickly grow and lead to MSTIDs.

Storm time expansion or penetration of high-latitude convection (Thomas & Shepherd, 2018; Zhang et al., 2007) into midlatitudes will have similar effects as SAPS in imposing poleward electric fields at midlatitudes and therefore will play a role in the MSTID development. As described in Section 1, SED plume is found to be related to the horizontal (sunward) flow related to SAPS as well as vertical and horizontal plasma flows due to PPEF. Among the events presented in this study, Case 1 demonstrated the SED and SAPS relationship via the strong poleward electric field; SEDs in Cases 2 and 3 are likely signatures of SAPS or PPEF, although direct electric field measurements of SAPS or PPEF were not available. Therefore, we speculate the MSTIDs result also from a storm time electric field induced Perkins instability, although it must be pointed out that other plasma instabilities (such as gradient drift instability, and Kelvin–Helmholtz instability) need additional clarification.

The intensity of electric fields associated with SAPS or PPEF and thermospheric responses are also hinted in the zonal neutral wind responses in Cases 2–4. In all those intervals with westward wind enhancements, the meridional wind enhancements were either too weak or lagged behind the zonal wind variations. Therefore, these westward wind enhancements were unlikely caused by the equatorward wind surge (originated by the auroral heating) via Coriolis forcing as part of DDEF processes. These were more likely associated with SAPS or PPEF which provided strong ion drag effects.

Enhanced storm-time PPEF, specifically the eastward electric field, was suggested to be associated with the Perkins instability leading to "super-MSTIDs" observed in Japanese longitudes at lower midlatitudes, ∼35°N geographic or ∼25°N magnetic latitudes, in the Nishioka et al. (2009) study. This eastward electric field has a similar effect as the poleward (SAPS) electric field in generating the Perkins instability where the effective electric field $\mathbf{E}_0^*$ must have a northward, eastward, or northeastward component to provide positive growth rates.

It is very interesting to note that the observed westward propagation of MSTIDs had similar speed as the westward wind in all the cases. This fact means that even though the MSTIDs **excitation** is benefited from large poleward electric fields such as SAPS and PPEF, the MSTID zonal **propagation** could be sustained because of the comparable disturbance zonal wind speed. In this scenario, the **bulk** plasma motion is westward as the neutral motion is, because of the poleward electric field generated by the westward disturbance wind as part of the midlatitude *F* region dynamo on the nightside (DDEF). The MSTID westward propagation was on top of the westward drifting of the bulk plasma which moves along with the neutrals. At high latitudes, the MSTIDs zonal propagation is also similarly affected by the background convection electric field (Shiokawa et al., 2012).

The above-mentioned consistence in the directions of the MSTID westward propagation and the westward background ion drift agrees with the Perkins instability theory in the *F* region. During nonstorm conditions at night, the westward propagation of MSTIDs is opposite to the background (eastward) *F* region ion drift driven by the neutral wind dynamo (e.g., Makela & Otsuka, 2011), unless the large electric field associated with the Es

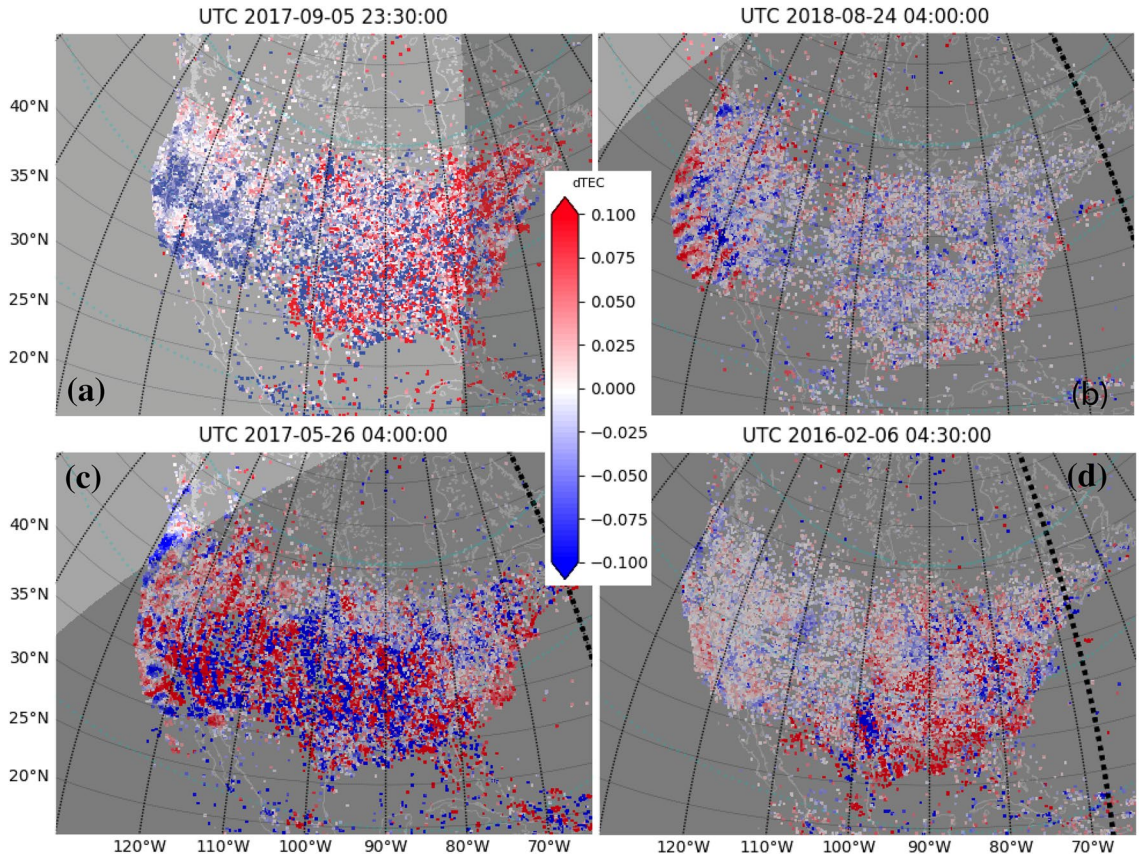

Figure 13. Sample medium-scale traveling ionospheric disturbances (MSTIDs) maps during nonstorm/non-substorm conditions corresponding approximately to the four storm periods: (a) 2017-09-05 23:30 UT, 2 days before Case 1; (b) 2018-08-24 04:00 UT, 1 day before Case 2; (c) 2017-05-26 04:00 UT, 3 days before Case 3; (d) 2016-02-06, 4 days after Case 4.

instability is involved via the *E–F* region coupling. Therefore, storm time electric fields with a poleward component can lead to the growth of *F* region Perkins instability, without invoking the Es instability, and thereby electrified MSTIDs which propagate westward, in the same direction as the background ion drift.

Finally, gravity waves (GWs) can also generate MSTIDs at midlatitudes. Storm time GWs/TADs excited by auroral processes are known for driving TIDs of various scale sizes, including MSTIDs, to propagate through midlatitudes (Hunsucker, 1982). These TIDs, however, are characterized with predominately equatorward propagation, unlike the zonally propagating MSTIDs in this study. In the DDEF theory, zonal wind disturbances responding to the equatorward wind surge (although not present in the cases we have examined as mentioned above) would carry poleward polarization electric fields and potentially have an impact on MSTID excitation and propagation at midlatitudes.

Meteorological and low atmosphere disturbances can excite GWs that will land in the ionosphere as primary GWs or provide body forcing and excite secondary GWs to generate concentric-type TIDs (Vadas & Azeem, 2021). The observed MSTIDs for the present study, however, are clearly not concentric. GWs near the terminator have often been observed, for example, Zhang, Erickson, Gasque, et al. (2021) identified eastward propagating electrified TIDs during postsunrise hours, and Figure 6 shows MSTIDs near the sunset terminator at 01:30 UT on 2018-08-26 (marked as T4). To provide further contrasts of MSTIDs between storm/substorm and non-storm/substorm conditions, Figure 13 depicts sample non-storm/non-substorm MSTIDs close to the periods of the four storm events studied here. Figure 13a corresponding to Case 1 had regional fluctuations near the dusk terminator, however, these structures were less organized and appeared to have concentric wavefronts. Figure 13b corresponding to Case 2 shows well-organized regional MSTIDs in the southern California which are a nominal disturbance feature (Kotake et al., 2007). Figure 13c corresponding to Case 3 appears to be MSTIDs spreading the southern CONUS with a clear circular boundary in the north. Figure 13d corresponding to Case 4 shows minor

disturbances in the northeast US that could be related to a minor elevation of AE index (~100–200 nT). Clearly, all these storm-irrelevant MSTIDs are quite different from the storm-induced MSTIDs in a variety of ways.

5. Summary

Geomagnetic storms and substorms can initiate a variety of TIDs; the present study focuses on the subauroral and midlatitude regions where the characteristic SED plume and SAPS develop. This paper provides the first observations of storm-time MSTIDs in the vicinity of the SED and SAPS at middle and subauroral latitudes using GNSS TEC data from the dense receiver networks in the CONUS during several intervals of recent geospace storms. MSTIDs there exhibited dramatic changes with the onset of SED/SAPS but eventually, they propagated away and impacted the surrounding ionosphere. Ionospheric ion drifts and thermospheric winds during the MSTID intervals are also analyzed using the ISR and FPI observations at Millstone Hill and midlatitude SuperDARN. These storms occurred on 2018-08-25/26, 2017-09-07/08, 2017-05-27/28, and 2016-02-02/03 with minimum SYM-H index −206, −146, −142, and −58 nT, respectively.

MSTIDs in these four cases were observed (a) during the intervals of IMF Bz being stably southward; (b) at night (from the dusk-to-midnight local times); (c) with multiple characteristic wavefronts often elongated in NW-SE, 2°–3° longitude apart, and westward propagating at a range of zonal phase speeds between 100 and 300 m/s; (d) initially in the northeastern US and being intensified or developed in the central US; (e) concurrent with the SED structure (especially the SED base region), or with other smaller electron density patches lagged behind (i.e., to the east of) the SED; (f) onset with the SAPS presence; (g) with zonal propagation being nearly synchronized with the elevated westward thermospheric wind.

We suggest several storm-time electric fields could be responsible for the MSTID excitation and subsequent propagation. An intense SAPS poleward electric field or penetration/expansion of the high-latitude convection electric field, both of which were signified by enhanced thermospheric westward winds, may be intense enough to trigger the Perkins instability with a sufficiently large linear growth rate. Enhanced westward winds continued to evolve, leaving the region of the strong ion–neutral coupling dominated by SAPS or penetration poleward electric field. Storm time neutral dynamics could also contribute to the enhanced thermospheric westward winds. These winds generated the polarization electric field via dynamo action at the nightside. The bulk of ions thus had westward drift which facilitated the westward propagation of MSTIDs. The consistent direction of westward ion drift and MSTID propagation agrees with the *F* region Perkins instability theory. Our discussion outlines a preliminary ionosphere–thermosphere–magnetosphere electrodynamical coupling framework to understand storm-time MSTIDs in the vicinity of the SED structure.

Data Availability Statement

GNSS TEC, Millstone Hill FPI, and ISR data are all available from Madrigal database (http://cedar.openmadrigal.org/openmadrigal/). Original line-of-sight TEC data can be found here: https://w3id.org/cedar?experiment_list=experiments2/2016/gps/02feb16%26file_list=los_20160202.001.h5, https://w3id.org/cedar?experiment_list=experiments2/2017/gps/07sep17%26file_list=los_20170907.004.h5, https://w3id.org/cedar?experiment_list=experiments2/2017/gps/25may17%26file_list=los_20170525.001.h5, and https://w3id.org/cedar?experiment_list=experiments4/2018/gps/25aug18%26file_list=los_20180825.001.h5. Millstone Hill ISR data here: https://w3id.org/cedar?experiment_list=experiments/2017/mlh/06sep17%26file_list=mlh170906g.003.hdf5 and https://w3id.org/cedar?experiment_list=experiments/2017/mlh/07sep17%26file_list=mlh170907g.003.hdf5. Millstone Hill Hi-Res FPI data can be downloaded from Madrigal too: https://w3id.org/cedar?experiment_list=experiments/2016/kfp/02feb16%26file_list=kfp160202g.7100.hdf5, https://w3id.org/cedar?experiment_list=experiments/2017/kfp/28may17%26file_list=kfp170527g.7100.hdf5, https://w3id.org/cedar?experiment_list=experiments/2016/kfp/26aug16%26file_list=kfp160825g.7100.hdf5. To download data from Madrigal using these URLs, the first time user will need to provide brief user information. The raw SuperDARN data used in this study are available from the British Antarctic Survey (BAS) SuperDARN data mirror (https://www.bas.ac.uk/project/superdarn). Solar wind and geomagnetic index data can be found from NASA OMNIWeb https://omniweb.gsfc.nasa.gov/form/omni_min.html. MSTID Animations for the four events are included in this paper as supplementary and also available at Github: https://github.com/shunrong-zhang/MSTIDs.

Acknowledgments
GNSS TEC processing, Millstone Hill incoherent scatter radar observations, and CEDAR Madrigal open-access database which archives these and FPI data used in this study are provided by the Massachusetts Institute of Technology's Haystack Observatory under support from US National Science Foundation (NSF) grant AGS-1952737. FPI operation is supported by NSF grant AGS-2030679. We acknowledge also the AFOSR MURI project ONR15-FOA-0011, ONR grant N00014-17-1-2186, NSF grants AGS-2033787, AGS-1907698, and AGS-2029840, and NASA LWS 80NSSC21K1310, 80NSSC21K1321, and 80NSSC18K0657. Data for TEC processing are provided from the following organizations: UNAVCO, Scripps Orbit and Permanent Array Center, Institut Geographique National, France, International GNSS Service, The Crustal Dynamics Data Information System (CDDIS), National Geodetic Survey, Instituto Brasileiro de Geografia e Estatística, RAMSAC CORS of Instituto Geográfico Nacional de la República Argentina, Arecibo Observatory, Low-Latitude Ionospheric Sensor Network (LISN), Topcon Positioning Systems, Inc., Canadian High Arctic Ionospheric Network, Institute of Geology and Geophysics, Chinese Academy of Sciences, China Meteorology Administration, Centro di Ricerche Sismologiche, Système d'Observation du Niveau des Eaux Littorales (SONEL), RENAG: REseau NAtional GPS permanent, GeoNet—the official source of geological hazard information for New Zealand, GNSS Reference Networks, Finnish Meteorological Institute, and SWEPOS—Sweden. We thank ISSI and ISSI-BJ for supporting the international team on "Multi-Scale Magnetosphere–Ionosphere–Thermosphere Interaction" which benefited greatly this study. We acknowledge using the UMass Lowell GIRO DIDBASE for browsing ionograms that also benefited this study. The authors acknowledge the use of SuperDARN data. SuperDARN is a collection of radars funded by the national scientific funding agencies of Australia, Canada, China, France, Italy, Japan, Norway, South Africa, United Kingdom, and the United States of America. Data from the Christmas Valley SuperDARN radars are provided under support from NSF grant AGS-1934997; data from the Blackstone and Fort Hays SuperDARN radars are provided under support from NSF grant AGS-1935110.

References

Aa, E., Zhang, S.-R., Erickson, P. J., Coster, A. J., Goncharenko, L. P., Varney, R. H., & Eastes, R. (2021). Salient midlatitude ionosphere–thermosphere disturbances associated with SAPS during a minor but geo-effective storm at deep solar minimum. *Journal of Geophysical Research: Space Physics*, *126*, e2021JA029509. https://doi.org/10.1029/2021JA029509

Aa, E., Zou, S., Ridley, A., Zhang, S.-R., Coster, A. J., Erickson, P. J., et al. (2019). Merging of storm time midlatitude traveling ionospheric disturbances and equatorial plasma bubbles. *Space Weather*, *17*, 285–298. https://doi.org/10.1029/2018SW002101

Belehaki, A., Tsagouri, I., Altadill, D., Blanch, E., Borries, C., Buresova, D., et al. (2020). An overview of methodologies for real-time detection, characterisation and tracking of traveling ionospheric disturbances developed in the TechTIDE project. *Journal of Space Weather and Space Climate*, *10*, 42. https://doi.org/10.1051/swsc/2020043

Blanc, M., & Richmond, A. D. (1980). The ionospheric disturbance dynamo. *Journal of Geophysical Research*, *85*(A4), 1669. https://doi.org/10.1029/JA085iA04p01669

Buonsanto, M. J. (1999). Ionospheric storms—A review. *Space Science Reviews*, *88*(3), 563–601. https://doi.org/10.1023/a:1005107532631

Chisham, G., Lester, M., Milan, S. E., Freeman, M. P., Bristow, W. A., Grocott, A., et al. (2007). A decade of the Super Dual Auroral Radar Network (SuperDARN): Scientific achievements, new techniques and future directions. *Surveys in Geophysics*, *28*(1), 33–109. https://doi.org/10.1007/s10712-007-9017-8

Cosgrove, R. B., & Tsunoda, R. T. (2004). Instability of the *E–F* coupled nighttime midlatitude ionosphere. *Journal of Geophysical Research*, *109*, A04305. https://doi.org/10.1029/2003JA010243

Coster, A., Herne, D., Erickson, P., & Oberoi, D. (2012). Using the Murchison Widefield Array to observe midlatitude space weather. *Radio Science*, *47*, RS0K07. https://doi.org/10.1029/2012RS004993

Coster, A. J., Goncharenko, L., Zhang, S.-R., Erickson, P. J., Rideout, W., & Vierinen, J. (2017). GNSS observations of ionospheric variations during the 21 August 2017 solar eclipse. *Geophysical Research Letters*, *44*, 12041–12048. https://doi.org/10.1002/2017GL075774

Deng, Y., & Ridley, A. J. (2006). Role of vertical ion convection in the high-latitude ionospheric plasma distribution. *Journal of Geophysical Research*, *111*, A09314. https://doi.org/10.1029/2006JA011637

Duly, T. M., Huba, J. D., & Makela, J. J. (2014). Self-consistent generation of MSTIDs within the SAMI3 numerical model. *Journal of Geophysical Research: Space Physics*, *119*, 6745–6757. https://doi.org/10.1002/2014JA020146

Emmert, J. T., Fejer, B. G., & Sipler, D. P. (2003). Climatology and latitudinal gradients of quiet time thermospheric neutral winds over Millstone Hill from Fabry–Perot interferometer measurements. *Journal of Geophysical Research*, *108*(A5), 1196. https://doi.org/10.1029/2002JA009765

England, S. L., Greer, K. R., Zhang, S.-R., Evans, S., Solomon, S. C., Eastes, R. W., et al. (2021). First comparison of traveling atmospheric disturbances observed in the middle thermosphere by Global-Scale Observations of the Limb and Disk to traveling ionospheric disturbances seen in ground-based total electron content observations. *Journal of Geophysical Research: Space Physics*, *126*, e2021JA029248. https://doi.org/10.1029/2021JA029248

Ferdousi, B., Nishimura, Y., Maruyama, N., & Lyons, L. R. (2019). Subauroral neutral wind driving and its feedback to SAPS during the 17 March 2013 geomagnetic storm. *Journal of Geophysical Research: Space Physics*, *124*, 2323–2337. https://doi.org/10.1029/2018JA026193

Foster, J. C. (1993). Storm time plasma transport at middle and high latitudes. *Journal of Geophysical Research*, *98*(A2), 1675–1689. https://doi.org/10.1029/92JA02032

Foster, J. C., & Burke, W. J. (2002). SAPS: A new categorization for sub-auroral electric fields. *Eos, Transactions American Geophysical Union*, *83*(36), 393. https://doi.org/10.1029/2002EO000289

Foster, J. C., Rideout, W., Sandel, B., Forrester, W. T., & Rich, F. J. (2007). On the relationship of SAPS to storm-enhanced density. *Journal of Atmospheric and Solar-Terrestrial Physics*, *69*(3), 303–313. https://doi.org/10.1016/j.jastp.2006.07.021

Foster, J. C., Zou, S., Heelis, R. A., & Erickson, P. J. (2021). Ionospheric storm-enhanced density plumes. In *Ionosphere dynamics and applications* (pp. 115–126). Washington, DC: American Geophysical Union (AGU). https://doi.org/10.1002/9781119815617.ch6

Francis, S. H. (1975). Global propagation of atmospheric gravity waves: A review. *Journal of Atmospheric and Terrestrial Physics*, *37*(6–7), 1011–1054. https://doi.org/10.1016/0021-9169(75)90012-4

Greenwald, R. A., Baker, K. B., Dudeney, J. R., Pinnock, M., Jones, T. B., Thomas, E. C., et al. (1995). DARN/SuperDARN: A global view of the dynamics of high-latitude convection. *Space Science Reviews*, *71*(1), 761–796. https://doi.org/10.1007/BF00751350

Guo, J. P., Deng, Y., Zhang, D. H., Lu, Y., Sheng, C., & Zhang, S.-R. (2018). The effect of subauroral polarization streams on ionosphere and thermosphere during the 2015 St. Patrick's Day storm: Global ionosphere–thermosphere model simulations. *Journal of Geophysical Research: Space Physics*, *123*, 2241–2256. https://doi.org/10.1002/2017JA024781

Heelis, R. A., Sojka, J. J., David, M., & Schunk, R. W. (2009). Storm time density enhancements in the middle-latitude dayside ionosphere. *Journal of Geophysical Research*, *114*, A03315. https://doi.org/10.1029/2008JA013690

Hocke, K., & Schlegel, K. (1996). A review of atmospheric gravity waves and travelling ionospheric disturbances: 1982–1995. *Annales Geophysicae*, *14*(9), 917–940. https://doi.org/10.1007/s00585-996-0917-6

Huang, C.-S. (2019). Long-lasting penetration electric fields during geomagnetic storms: Observations and mechanisms. *Journal of Geophysical Research: Space Physics*, *124*, 9640–9664. https://doi.org/10.1029/2019JA026793

Hunsucker, R. D. (1982). Atmospheric gravity waves generated in the high-latitude ionosphere: A review. *Reviews of Geophysics*, *20*(2), 293–315. https://doi.org/10.1029/RG020i002p00293

Jaggi, R. K., & Wolf, R. A. (1973). Self-consistent calculation of the motion of a sheet of ions in the magnetosphere. *Journal of Geophysical Research*, *78*(16), 2852–2866. https://doi.org/10.1029/JA078i016p02852

Jonah, O. F., Coster, A., Zhang, S.-R., Goncharenko, L. M., Erickson, P. J., de Paula, E. R., & Kherani, E. A. (2018). TID observations and source analysis during the 2017 Memorial Day weekend geomagnetic storm over North America. *Journal of Geophysical Research: Space Physics*, *42*, 7874. https://doi.org/10.1029/2018JA025367

Kelley, M. C. (2011). On the origin of mesoscale TIDs at midlatitudes. *Annales Geophysicae*, *29*(2), 361–366. https://doi.org/10.5194/angeo-29-361-2011

Kelley, M. C., Fejer, B. G., & Gonzales, C. A. (1979). An explanation for anomalous equatorial ionospheric electric fields associated with a northward turning of the interplanetary magnetic field. *Geophysical Research Letters*, *6*(4), 301–304. https://doi.org/10.1029/GL006i004p00301

Kerr, R. (2019). Measurement of thermospheric vertical neutral winds with a single etalon Fabry–Perot interferometer. In *AGU Fall Meeting Abstracts*.

Kil, H., & Paxton, L. J. (2017). Global distribution of nighttime medium-scale traveling ionospheric disturbances seen by Swarm satellites. *Geophysical Research Letters*, *44*, 9176–9182. https://doi.org/10.1002/2017GL074750

Kotake, N., Otsuka, Y., Ogawa, T., Tsugawa, T., & Saito, A. (2007). Statistical study of medium-scale traveling ionospheric disturbances observed with the GPS networks in Southern California. *Earth, Planets and Space*, *59*(2), 95–102. https://doi.org/10.1186/bf03352681

Liu, C. H., & Yeh, K. C. (1969). Effect of ion drag on propagation of acoustic-gravity waves in the atmospheric *F* region. *Journal of Geophysical Research*, *74*(9), 2248–2255. https://doi.org/10.1029/JA074i009p02248

Liu, J., Wang, W., Burns, A., Solomon, S. C., Zhang, S.-R., Zhang, Y., & Huang, C. (2016). Relative importance of horizontal and vertical transports to the formation of ionospheric storm-enhanced density and polar tongue of ionization. *Journal of Geophysical Research: Space Physics*, *121*, 8121–8133. https://doi.org/10.1002/2016JA022882

Lu, G., Richmond, A. D., Lühr, H., & Paxton, L. (2016). High-latitude energy input and its impact on the thermosphere. *Journal of Geophysical Research: Space Physics*, *121*, 7108–7124. https://doi.org/10.1002/2015JA022294

Lu, G., Zakharenkova, I., Cherniak, I., & Dang, T. (2020). Large-scale ionospheric disturbances during the 17 March 2015 storm: A model-data comparative study. *Journal of Geophysical Research: Space Physics*, *125*, 333. https://doi.org/10.1029/2019JA027726

Lyons, L. R., Nishimura, Y., Zhang, S.-R., Coster, A., Liu, J., Bristow, W. A., et al. (2021). Direct connection between auroral oval streamers/flow channels and equatorward traveling ionospheric disturbances. *Frontiers in Astronomy and Space Sciences*, *8*, 738507. https://doi.org/10.3389/fspas.2021.738507

Lyons, L. R., Nishimura, Y., Zhang, S.-R., Coster, A. J., Bhatt, A., Kendall, E., & Deng, Y. (2019). Identification of auroral zone activity driving large-scale traveling ionospheric disturbances. *Journal of Geophysical Research: Space Physics*, *124*, 700–714. https://doi.org/10.1029/2018JA025980

Makela, J. J., & Otsuka, Y. (2011). Overview of nighttime ionospheric instabilities at low- and mid-latitudes: Coupling aspects resulting in structuring at the mesoscale. *Space Science Reviews*, *168*(1–4), 419–440. https://doi.org/10.1007/978-1-4614-5677-3_14

Martinis, C., Baumgardner, J., Wroten, J., & Mendillo, M. (2011). All-sky imaging observations of conjugate medium-scale traveling ionospheric disturbances in the American sector. *Journal of Geophysical Research*, *116*, A05326. https://doi.org/10.1029/2010JA016264

Mendillo, M. (2006). Storms in the ionosphere: Patterns and processes for total electron content. *Reviews of Geophysics*, *44*, RG4001. https://doi.org/10.1029/2005RG000193

Narayanan, V., Shiokawa, K., Otsuka, Y., & Neudegg, D. (2018). On the role of thermospheric winds and sporadic e layers in the formation and evolution of electrified MSTIDs in geomagnetic conjugate regions. *Journal of Geophysical Research: Space Physics*, *123*, 6957–6980. https://doi.org/10.1029/2018JA025261

Nishida, A. (1968). Coherence of geomagnetic DP 2 fluctuations with interplanetary magnetic variations. *Journal of Geophysical Research*, *73*, 5549–5559. https://doi.org/10.1029/JA073i017p05549

Nishimura, Y., Zhang, S.-R., Lyons, L. R., Deng, Y., Coster, A. J., Moen, J. I., et al. (2020). Source region and propagation of dayside large-scale traveling ionospheric disturbances. *Geophysical Research Letters*, *47*, e2020GL089451. https://doi.org/10.1029/2020GL089451

Nishioka, M., Saito, A., & Tsugawa, T. (2009). Super-medium-scale traveling ionospheric disturbance observed at midlatitude during the geomagnetic storm on 10 November 2004. *Journal of Geophysical Research*, *114*, A07310. https://doi.org/10.1029/2008JA013581

Nishitani, N., Ruohoniemi, J. M., Lester, M., Baker, J. B. H., Koustov, A. V., Shepherd, S. G., et al. (2019). Review of the accomplishments of mid-latitude Super Dual Auroral Radar Network (SuperDARN) HF radars. *Progress in Earth and Planetary Science*, *6*, 27. https://doi.org/10.1186/s40645-019-0270-5

Otsuka, Y., Shiokawa, K., Ogawa, T., & Wilkinson, P. (2004). Geomagnetic conjugate observations of medium-scale traveling ionospheric disturbances at midlatitude using all-sky airglow imagers. *Geophysical Research Letters*, *31*, L15803. https://doi.org/10.1029/2004GL020262

Otsuka, Y., Suzuki, K., Nakagawa, S., Nishioka, M., Shiokawa, K., & Tsugawa, T. (2013). GPS observations of medium-scale traveling ionospheric disturbances over Europe. *Annales Geophysicae*, *31*(2), 163–172. https://doi.org/10.5194/angeo-31-163-2013

Perkins, F. (1973). Spread F and ionospheric currents. *Journal of Geophysical Research*, *78*(1), 218–226. https://doi.org/10.1029/JA078i001p00218

Richmond, A. D. (1978). Gravity wave generation, propagation, and dissipation in the thermosphere. *Journal of Geophysical Research*, *83*(A9), 4131–4145. https://doi.org/10.1029/JA083iA09p04131

Rideout, W., & Coster, A. (2006). Automated GPS processing for global total electron content data. *GPS Solutions*, *10*(3), 219–228. https://doi.org/10.1007/s10291-006-0029-5

Saito, A., Fukao, S., & Miyazaki, S. (1998). High resolution mapping of TEC perturbations with the GSI GPS Network over Japan. *Geophysical Research Letters*, *25*(16), 3079–3082. https://doi.org/10.1029/98GL52361

Saito, S., Yamamoto, M., Hashiguchi, H., Maegawa, A., & Saito, A. (2007). Observational evidence of coupling between quasi-periodic echoes and medium scale traveling ionospheric disturbances. *Annales Geophysicae*, *25*, 2185–2194. https://doi.org/10.5194/angeo-25-2185-2007

Savitzky, A., & Golay, M. J. E. (1964). Smoothing and differentiation of data by simplified least squares procedures. *Analytical Chemistry*, *36*, 1627–1639. https://doi.org/10.1021/ac60214a047

Sheng, C., Deng, Y., Zhang, S.-R., Nishimura, Y., & Lyons, L. R. (2020). Relative contributions of ion convection and particle precipitation to exciting large-scale traveling atmospheric and ionospheric disturbances. *Journal of Geophysical Research: Space Physics*, *125*, e2019JA027342. https://doi.org/10.1029/2019JA027342

Shiokawa, K. (2003). Ground and satellite observations of nighttime medium-scale traveling ionospheric disturbance at midlatitude. *Journal of Geophysical Research*, *108*(A4), 1145. https://doi.org/10.1029/2002JA009639

Shiokawa, K., Ihara, C., Otsuka, Y., & Ogawa, T. (2002). Statistical study of nighttime medium-scale traveling ionospheric disturbances using midlatitude airglow images. *Journal of Geophysical Research*, *108*(A1), 1052. https://doi.org/10.1029/2002JA009491

Shiokawa, K., Mori, M., Otsuka, Y., Oyama, S., & Nozawa, S. (2012). Motion of high-latitude nighttime medium-scale traveling ionospheric disturbances associated with auroral brightening. *Journal of Geophysical Research*, *117*, A10316. https://doi.org/10.1029/2012JA017928

Thomas, E. G., & Shepherd, S. G. (2018). Statistical patterns of ionospheric convection derived from mid-latitude, high-latitude, and polar SuperDARN HF radar observations. *Journal of Geophysical Research: Space Physics*, *123*, 3196–3216. https://doi.org/10.1002/2018JA025280

Tsugawa, T., Kotake, N., Otsuka, Y., & Saito, A. (2007). Medium-scale traveling ionospheric disturbances observed by GPS receiver network in Japan: A short review. *GPS Solutions*, *11*(2), 139–144. https://doi.org/10.1007/s10291-006-0045-5

Vadas, S. L., & Azeem, I. (2021). Concentric secondary gravity waves in the thermosphere and ionosphere over the continental United States on March 25–26, 2015 from deep convection. *Journal of Geophysical Research: Space Physics*, *126*, e2020JA028275. https://doi.org/10.1029/2020JA028275

Valladares, C. E., & Sheehan, R. (2016). Observations of conjugate MSTIDs using networks of GPS receivers in the American sector. *Radio Science*, *51*, 1470–1488. https://doi.org/10.1002/2016RS005967

Vierinen, J., Coster, A. J., Rideout, W. C., Erickson, P. J., & Norberg, J. (2016). Statistical framework for estimating GNSS bias. *Atmospheric Measurement Techniques*, *9*, 1303–1312. https://doi.org/10.5194/amt-9-1303-2016

Wang, H., Lühr, H., Häusler, K., & Ritter, P. (2011). Effect of subauroral polarization streams on the thermosphere: A statistical study. *Journal of Geophysical Research*, *116*, A03312. https://doi.org/10.1029/2010JA016236

Wang, W., Talaat, E. R., Burns, A. G., Emery, B., Hsieh, S.-Y., Lei, J., & Xu, J. (2012). Thermosphere and ionosphere response to subauroral polarization streams (SAPS): Model simulations. *Journal of Geophysical Research*, *117*, A07301. https://doi.org/10.1029/2012JA017656

Yeh, K. C., & Liu, C. H. (1974). Acoustic-gravity waves in the upper atmosphere. *Reviews of Geophysics*, *12*(2), 193. https://doi.org/10.1029/RG012i002p00193

Yokoyama, T. (2013). Scale dependence and frontal formation of nighttime medium-scale traveling ionospheric disturbances. *Geophysical Research Letters*, *40*, 4515–4519. https://doi.org/10.1002/grl.50905

Yokoyama, T., Hysell, D. L., Otsuka, Y., & Yamamoto, M. (2009). Three-dimensional simulation of the coupled Perkins and es-layer instabilities in the nighttime midlatitude ionosphere. *Journal of Geophysical Research*, *114*, A03308. https://doi.org/10.1029/2008JA013789

Zhang, S.-R. (2021). Large-scale traveling ionospheric disturbances . In Y. Nishimura, O. Verkhoglyadova, Y. Deng, & S.-R. Zhang (Eds.), *Cross-scale coupling and energy transfer in the magnetosphere–ionosphere–thermosphere system* (pp. 482–499). Amsterdam, The Netherlands: Elsevier.

Zhang, S.-R., & Aa, E. (2021). Ionospheric electron density large gradients at midlatitudes. In Y. Nishimura, O. Verkhoglyadova, Y. Deng, & S.-R. Zhang (Eds.), *Cross-scale coupling and energy transfer in the magnetosphere–ionosphere–thermosphere system* (pp. 175–193). Amsterdam, The Netherlands: Elsevier.

Zhang, S.-R., Coster, A. J., Erickson, P. J., Goncharenko, L. P., Rideout, W., & Vierinen, J. (2019). Traveling ionospheric disturbances and ionospheric perturbations associated with solar flares in September 2017. *Journal of Geophysical Research: Space Physics*, *60*, 895. https://doi.org/10.1029/2019JA026585

Zhang, S.-R., Erickson, P. J., Coster, A. J., Rideout, W., Vierinen, J., Jonah, O., & Goncharenko, L. P. (2019). Subauroral and polar traveling ionospheric disturbances during the 7–9 September 2017 storms. *Space Weather*, *17*, 1748–1764. https://doi.org/10.1029/2019SW002325

Zhang, S.-R., Erickson, P. J., Foster, J. C., Holt, J. M., Coster, A. J., Makela, J. J., et al. (2015). Thermospheric poleward wind surge at midlatitudes during great storm intervals. *Geophysical Research Letters*, *42*, 5132–5140. https://doi.org/10.1002/2015GL064836

Zhang, S.-R., Erickson, P. J., Gasque, L. C., Aa, E., Rideout, W., Vierinen, J., et al. (2021). Electrified postsunrise ionospheric perturbations at Millstone Hill. *Geophysical Research Letters*, *48*, e2021GL095151. https://doi.org/10.1029/2021GL095151

Zhang, S.-R., Erickson, P. J., Goncharenko, L. P., Coster, A. J., Rideout, W., & Vierinen, J. (2017). Ionospheric bow waves and perturbations induced by the 21 August 2017 solar eclipse. *Geophysical Research Letters*, *44*, 12067–12073. https://doi.org/10.1002/2017GL076054

Zhang, S.-R., Erickson, P. J., Vierinen, J., Aa, E., Rideout, W., Coster, A. J., & Goncharenko, L. P. (2021). Conjugate ionospheric perturbation during the 2017 solar eclipse. *Journal of Geophysical Research: Space Physics*, *126*, e2020JA028531. https://doi.org/10.1029/2020JA028531

Zhang, S.-R., Holt, J. M., & McCready, M. (2007). High latitude convection based on long-term incoherent scatter radar observations in North America. *Journal of Atmospheric and Solar-Terrestrial Physics*, *69*(10–11), 1273–1291. https://doi.org/10.1016/j.jastp.2006.08.017

Zhang, S.-R., Vierinen, J., Aa, E., Goncharenko, L. P., Erickson, P. J., Rideout, W., et al. (2022). 2022 Tonga volcanic eruption induced global propagation of ionospheric disturbances via Lamb waves. *Frontiers in Astronomy and Space Sciences*, *9*, 871275. https://doi.org/10.3389/fspas.2022.871275

Zhou, Q., & Mathews, J. D. (2006). On the physical explanation of the Perkins instability. *Journal of Geophysical Research*, *111*, A12309. https://doi.org/10.1029/2006JA011696

Zou, S., Moldwin, M. B., Ridley, A. J., Nicolls, M. J., Coster, A. J., Thomas, E. G., & Ruohoniemi, J. M. (2014). On the generation/decay of the storm-enhanced density plumes: Role of the convection flow and field-aligned ion flow. *Journal of Geophysical Research: Space Physics*, *119*, 8543–8559. https://doi.org/10.1002/2014JA020408